Monthly Notices
of the
ROYAL ASTRONOMICAL SOCIETY

MNRAS **546**, 1–24 (2026) https://doi.org/10.1093/mnras/stag025
Advance Access publication 2026 January 10

Intensive X-Ray/UVOIR continuum reverberation mapping of the Seyfert AGN MCG +08–11–11

D. Kynoch,[1,2★] I. M. M^{c}Hardy,[1] E. M. Cackett,[3] J. Gelbord,[4] J. V. Hernández Santisteban,[5] K. Horne,[5] J. A. Miller,[3,6] H. Netzer,[7] C. Done,[8] R. Edelson,[9] M. M. Fausnaugh,[10] M. R. Goad,[11] B. M. Peterson[12] and F. M. Vincentelli[1,13]

[1] *School of Physics and Astronomy, University of Southampton, University Road, Southampton SO17 1BJ, UK*
[2] *Institute of Cosmology and Gravitation, University of Portsmouth, Burnaby Road, Portsmouth PO1 3FX, UK*
[3] *Department of Physics and Astronomy, Wayne State University, 666 W. Hancock St, Detroit, MI, 48201, USA*
[4] *Spectral Sciences Inc., 4 Fourth Avenue, Burlington, MA 01803, USA*
[5] *SUPA School of Physics and Astronomy, University of St Andrews, North Haugh, St Andrews KY16 9SS, UK*
[6] *Department of Physics & Astronomy, Texas A&M University, 400 Bizzell St, College Station, TX 77845, USA*
[7] *School of Physics and Astronomy, Tel Aviv University, Tel Aviv 69978, Israel*
[8] *Department of Physics, Centre for Extragalactic Astronomy, University of Durham, South Road, Durham DH1 3LE, UK*
[9] *Eureka Scientific Inc., 2452 Delmer St. Suite 100, Oakland, CA 94602, USA*
[10] *Department of Physics & Astronomy, Texas Tech University, Lubbock, TX 79409-1051, USA*
[11] *Department of Physics and Astronomy, College of Science and Engineering, University of Leicester, University Road, Leicester LE1 7RH, UK*
[12] *Retired*
[13] *INAF Istituto di Astrofisica e Planetologia Spaziali, Via del Fosso del Cavaliere 100, I-00133 Roma, Italy*

Accepted 2025 December 17. Received 2025 November 11; in original form 2025 June 27

ABSTRACT

We present results from intensive ($\times 3$ daily) 3-month-long X-ray, UV, and optical monitoring of the bright Seyfert active galactic nucleus (AGN) MCG +08–11–11 with *Swift*, supported by optical–infrared ground-based monitoring. The 12 resultant well-sampled light curves are highly correlated; the X-ray-to-UV correlation $r_{\rm max} = 0.85$ is the highest yet recorded in a Seyfert galaxy. The lags increase with wavelength, as expected from reprocessing of central high-energy emission by surrounding material. Our lag spectrum is much shallower than that obtained from an optical monitoring campaign conducted a year earlier, when MCG +08–11–11 was approximately four times brighter. After filtering out long-term trends in the earlier optical light curves we recover shorter lags consistent with our own, demonstrating concurrent reverberation signals from different spatial scales and the luminosity dependence of the measured lags. We use our lag spectrum to test several physical models, finding that disc reprocessing models cannot account for the observed 'excess' lags in the u and r–i bands that are highly indicative of the Balmer and Paschen continua produced by reprocessing in the broad-line region (BLR) gas. The structure seen in both the variable (rms) and lag spectra, and the large time delay between X-ray and UV variations (≈ 2 d) suggest that the BLR is the dominant reprocessor. The hard X-ray spectrum ($\Gamma \approx 1.7$) and faint red UV–optical spectrum indicate that the Eddington accretion ratio is low: $\dot{m}_{\rm E} \sim 0.03$. The bolometric luminosity then requires that the black hole mass is substantially greater than current reverberation mapping estimates.

Key words: accretion, accretion discs – galaxies: active – galaxies: individual: MCG + 08–11–11 – galaxies: Seyfert.

1 INTRODUCTION

Determining the inner structure of active galactic nuclei (AGN), and how that structure might vary with parameters such as black hole mass and accretion rate, is a topic of major importance in astrophysics. However, with the exceptions of M87 and Sgr A$*$, whose very inner regions have been mapped by very high-resolution radio interferometry (Event Horizon Telescope Collaboration 2019, 2022), almost all other AGN are too small for their structures to be determined by direct imaging. A more widely applicable indirect method of determining AGN inner structures is 'reverberation mapping' (RM; J. N. Bahcall, B.-Z. Kozlovsky & E. E. Salpeter 1972; R. D. Blandford & C. F. McKee 1982). Under the assumption that low-energy photons are produced by reprocessing of high-energy photons from near the black hole, by surrounding material, the structure of that material can be deduced from the time lags between wavebands.

RM was first envisaged as a means to probe the size scale and geometry of line-emitting gas (i.e. the broad-line region or BLR gas) by measuring the delayed response of emission lines to variations in the photoionizing UV continuum, assumed to come

---

★ E-mail: daniel.kynoch@port.ac.uk

from the inner accretion disc, very close to the black hole (e.g. B. M. Peterson 1993; B. M. Peterson et al. 2004). More recently, high-cadence photometric monitoring campaigns have concentrated on measuring the lags between the continuum X-ray and UV, optical and infrared (UVOIR) wavebands (e.g. I. M. M$^{\rm c}$Hardy et al. 2014, 2018; B. J. Shappee et al. 2014; R. Edelson et al. 2015, 2019; E. M. Cackett et al. 2018; E. M. Cackett, M. C. Bentz & E. Kara 2021, and many others). The lags have been compared with the expectations from reprocessing on a variety of surrounding structures. Until recently, the standard paradigm has been that the dominant reprocessor was the accretion disc around the black hole, usually assumed to have the temperature profile described by N. I. Shakura & R. A. Sunyaev (1973), which depends on the black hole mass ($M_{\rm BH}$), spin ($a_\star$), and accretion rate (which is commonly expressed as the ratio between an AGN's bolometric luminosity and its Eddington luminosity, i.e. $\dot{m}_{\rm E} \equiv L_{\rm bol}/L_{\rm Edd}$). However, although the lags (τ) usually increase with wavelength (λ) roughly in agreement with the expectation of disc reprocessing of $\tau \propto \lambda^{4/3}$ (E. M. Cackett, K. Horne & H. Winkler 2007), there are a number of discrepancies.

First, the lags should depend on the size and structure of the central X-ray source. However, under the assumption that this source can be approximated by a lamppost geometry, with a height of $\sim 10\ R_{\rm g}$, similar to that deduced from X-ray intraband reverberation (e.g. D. Emmanoulopoulos et al. 2014), the observed lags usually exceed the theoretical expectations, leading to speculation that perhaps the disc is clumpy, not smooth (I. M. M$^{\rm c}$Hardy et al. 2014). Numerical disc modelling (e.g. I. M. M$^{\rm c}$Hardy et al. 2014, 2018) usually leads to smaller discrepancies (factor ~ 2) than analytic formulae (factor 3 or greater, e.g. M. M. Fausnaugh et al. 2016; R. Edelson et al. 2019). More detailed disc modelling, including general relativistic effects, larger X-ray source heights ($> 10\ R_{\rm g}$), and a large disc colour temperature correction, suggests that there is no discrepancy (e.g. E. S. Kammoun et al. 2021) – although these models have not yet been fully explored.

Secondly, the lag between the X-rays and the near UV is usually factors of at least 5 greater than the lag expected from extrapolation of the lag spectrum between the optical and UV down to X-ray wavelengths (e.g. I. M. M$^{\rm c}$Hardy et al. 2018). However, that extrapolation is based on the assumption that a relationship of the form $\tau \propto \lambda^{4/3}$ describes the true shape of the lag spectrum. It has been shown that if there is an edge to the reprocessing region of the disc, perhaps caused by a disc wind arising at large radii that obscures the outer part of the disc, then the lag spectrum will flatten at long wavelengths (I. M. M$^{\rm c}$Hardy et al. 2023). Thus an extrapolation of the long-wavelength lag spectrum to short wavelengths will naturally lead to an apparent X-ray to UV lag excess.

Thirdly, although the UVOIR bands are always well correlated with each other, the correlation with the X-ray band is much weaker and sometimes no UV–X-ray correlation is found (e.g. E. Kara et al. 2021). For example, in a study of 21 AGN with *Swift* X-ray and UV data, a statistically significant correlation between the X-ray and UV light curves was found in only nine AGN (D. J. K. Buisson et al. 2017). However, I. M. M$^{\rm c}$Hardy et al. (2014) and M. Pahari et al. (2020) noted that removal of long-term trends in light curves, as recommended by W. F. Welsh (1999), can lead to stronger correlations and a much clearer detection of a reprocessing signature in the lags. Also, C. Panagiotou, E. Kara & M. Dovčiak (2022) showed that a corona with varying height will reduce the X-ray/UVOIR correlation strength while maintaining the basic principles of the lamppost model. E. Gardner & C. Done (2017) suggested that an inflated inner disc might scatter and delay the hard X-ray photons, which are then reprocessed into soft X-ray/far-UV photons, which then illuminate the rest of the disc. Thus an additional delay is added to the hard X-ray/UVOIR lag and the hard X-ray/UVOIR correlation is diluted.

Fourthly, the lags, particularly in the *u* band (e.g. E. M. Cackett et al. 2018) but also, to a lesser extent, in the *i* band (e.g. J. A. Miller et al. 2023), are larger than expected compared to the lags in surrounding bands. These lags probably arise from a contribution to the light in those wavebands from Balmer and Paschen continua, respectively, caused by reprocessing in the more distant BLR (K. T. Korista & M. R. Goad 2001, 2019). Frequency-resolved lag analyis also suggests a response originating from larger size scales, consistent with the BLR (E. M. Cackett, A. Zoghbi & O. Ulrich 2022; C. Lewin et al. 2023). The questions now are what fraction of the reprocessed light comes from the BLR (possibly all?: H. Netzer 2022); and, does that fraction vary between AGN?

There are also other questions concerning reprocessing from a disc. For example, why are the UV/optical light curves so smooth, compared to the X-rays? For MR 2251–178 P. Arévalo et al. (2008) show that an X-ray source height of 100 $R_{\rm g}$ is required to produce smooth enough optical light curves. However, such a height leads to larger X-ray to optical lags than are observed. The more rapidly varying X-ray light curves also lead to low peak X-ray/optical cross-correlation coefficients, although some smoothing of the X-ray light curves can increase the peak coefficient (E. M. Cackett et al. 2020).

To be able to discriminate between different physical models for the origin of the variability, and hence obtain a good understanding of the inner structures of AGN via RM, it is necessary to measure the lags between wavebands with high accuracy. Measurements with large uncertainty are not really very useful. Thus it is necessary to observe AGN that are very bright across all wavebands from X-ray to near-IR and that have established patterns of variability showing large-amplitude variations on time-scales that are well suited to the existing observational facilities. The target of the present investigation, MCG +08–11–11, fulfils these criteria extremely well, as we describe below.

1.1 The source MCG +08–11–11

The subject of this study is the bright nearby ($z = 0.0205$) Seyfert galaxy MCG +08–11–11 (also known as UGC 3374). It contains an X-ray bright nucleus and was the first Seyfert galaxy to be discovered by its X-ray emission (J. Ward et al. 1977). It is known to be strongly variable over all X-ray, UV, and optical wavebands.

In several spectroscopic observations made since 2004 MCG +08–11–11 has been shown to have a flat X-ray spectrum ($\Gamma \approx 1.8$; estimated over various energy bands between 0.5 and 150 keV; G. Matt et al. 2006; S. Bianchi et al. 2010; A. R. Patrick et al. 2012; K. D. Murphy & M. A. Nowak 2014; A. Tortosa et al. 2018). G. Matt et al. (2006) measured the X-ray flux (2–10 keV, unabsorbed) as 4.63×10^{-11} erg s^{-1} cm^{-2}, corresponding to a luminosity $\log(L_{\rm X}/{\rm erg\,s^{-1}}) = 43.6$. MCG +08–11–11 is bright in even hard X-rays (14–195 keV) and has been detected by *Swift*-BAT, with its luminosity reported as $\log(L_{\rm X}/{\rm erg\,s^{-1}}) = 44.13$ (A. Y. Lien et al. 2025).[1] It is known to be variable in X-rays over a range of time-scales: significant variability of its X-ray flux over

---

[1] *Swift* BAT 157-month hard X-ray survey: https://swift.gsfc.nasa.gov/results/bs157mon/

a period of 18 months was detected by the *Ariel V* Sky Survey Instrument (B. A. Cooke et al. 1978) and modest variability on shorter time-scales ($\sim$ 10 per cent variability in 38 ks) was detected in an *XMM–Newton* observation in 2004 (G. Matt et al. 2006).

In the optical, MCG +08–11–11 is a bright (V $\approx$ 14.2 mag) AGN, spectroscopically classified as a Seyfert 1.5 (having broad and narrow emission lines of comparable strength; D. E. Osterbrock & J. M. Shuder 1982). Its high optical brightness and variability have made the source an ideal target for both photometric and spectroscopic RM campaigns (e.g. S. G. Sergeev et al. 2005; M. M. Fausnaugh et al. 2017, 2018; C. Fian et al. 2023). M. M. Fausnaugh et al. (2017) reported a black hole mass of 2.82×10^7 M$_\odot$, derived from optical line reverberation, with an optical continuum-H β lag of $\approx$ 15 d. They note a factor of 3 uncertainty in the mass. The H β lag is in excellent agreement with the expectation based on its 5100 Å luminosity and the BLR radius–luminosity relation of M. C. Bentz et al. (2013). Q. Ma et al. (2023) determine a very similar lag for H α ($\approx$ 17 d) from photometric monitoring data. The Eddington accretion ratio, $\dot{m}_{\rm E}$, is less certain. From the 5100 Å luminosity, and assuming a bolometric correction factor of 10 and a mass of 2.82×10^7 M$_\odot$, M. M. Fausnaugh et al. (2018) report $\dot{m}_{\rm E} = 0.054$. However, from CREAM modelling of the optical light curves, the same authors report $\dot{m}_{\rm E} = 0.234$. We return to this point in Section 4.

MCG +08–11–11 has been the subject of previous optical continuum RM studies, which show it to be highly variable on ~few day to month time-scales across all optical bands. S. G. Sergeev et al. (2005) presented lag measurements between the *B* and *V*, *R* and *I* bands based on a $\sim$ 2-yr campaign beginning in 2001, with 69 sets of observations and typical sampling of $\sim$ 3 d. They find roughly wavelength-dependent lags with the *R* band lagging the *B* band by about 5 d. M. M. Fausnaugh et al. (2018) measured lags between the *ugriz* and 5100 Å bands. Their total number of observations is slightly fewer than those of S. G. Sergeev et al. (2005), but with better sampling of $\sim$ 1 d. They also find roughly wavelength-dependent lags, but shorter than those of S. G. Sergeev et al., with the *i* band lagging the *g* band by $\sim$ 1.5 d. Most recently, C. Fian et al. (2023) presented results from optical photometric monitoring of MCG +08–11–11 with approximately nightly cadence over 6 months in 2019–20 with the C18 telescope at the Wise Observatory. They robustly detected wavelength-dependent optical interband lags of up to 7 d (at 8025 Å relative to 4250 Å). They noted that the measured wavelength dependence of these lags, $\tau \propto \lambda^{4.74}$, is very much steeper than the $\tau \propto \lambda^{4/3}$ predicted for a standard thin accretion disc. Furthermore, the long lags imply an accretion disc approximately three to seven times larger than predicted by standard thin disc theory.

The observations discussed above show that MCG +08–11–11 is indeed a very bright AGN across all optical wavebands and that with a more intense observing campaign, it was very likely that good enough lags could be measured to allow for accurate modelling. However, none of those studies included contemporaneous X-ray observations, which are essential for proper modelling of the emission geometry, since in the disc reverberation paradigm it is the X-rays that drive short-time-scale variability at longer wavelengths. In this paper, we present the results from just such an RM campaign, covering a very wide range of wavelengths from X-rays to near-IR, over a 3-month period, with much more intensive sampling (better than twice daily) than previous studies.

This paper is structured as follows. In Section 2 we describe the observations of MCG +08–11–11, including our new *Swift*, Las Cumbres Observatory (LCO), and Zowada data. In Section 3 we perform timing analyses to assess the target's variability properties and determine its lag spectrum, $\tau(\lambda)$. In Section 4 we investigate the multiwavelength spectral energy distribution (SED) of the source and estimate its Eddington accretion ratio, $\dot{m}_{\rm E}$. In Section 5, informed by our SED and $\dot{m}_{\rm E}$ estimate, we model $\tau(\lambda)$ with thin-disc (5.1), flared-disc (5.2), and radiation-pressure-confined (RPC) cloud (5.3) models. Finally, in Section 6 we discuss our findings, and in Section 7 we summarize our conclusions.

2 OBSERVATIONS

2.1 2020-21 continuum reverberation mapping campaign

The structural conclusions regarding MCG +08–11–11, which we present later in this paper (Sections 4 and 5) are based on timing analysis (Section 3) of light curves obtained during a major co-ordinated monitoring campaign on MCG +08–11–11 conducted between 2020 January and 2021 November. In this section we describe these data.

The principal observations were obtained by the *Neil Gehrels Swift Observatory* (hereafter *Swift*) in a period of intensive monitoring between 2021 February and May (Section 2.1.1), although the source has been regularly monitored by *Swift* with low cadence for several months both before and after this period. The *Swift* observations were supported by ground-based optical-IR photometric monitoring conducted by the LCO network (Section 2.1.2) and the Dan Zowada Memorial Observatory (Section 2.1.3). Regular ground-based observations were conducted over the whole 2020–21 season when the target was at sufficiently low airmass during the night; the last 3 months of the ground observing seasons coincided with the intensive *Swift* monitoring period. In this work we have also made use of archival data from the *NuSTAR* and *XMM–Newton* Observatories, as described in Section 2.2.1 and 2.2.2, respectively. A forthcoming paper (Keeley et al. in preparation) will present an analysis of the longer term variability of MCG +08–11–11. In this paper we focus on the 3-month period of intensive *Swift* monitoring.

2.1.1 *Neil Gehrels Swift Observatory*

The *Swift* satellite is equipped with an X-ray Telescope (XRT; D. N. Burrows et al. 2005) and Ultra-Violet/Optical Telescope (UVOT; P. W. A. Roming et al. 2005; T. S. Poole et al. 2008). As summarized in Table 1, MCG +08–11–11 was intensively monitored by *Swift* between 2021 February 7 and May 7, with three visits per day during this 3-month period (Cycle 17 proposal 1720061; PI M$^{\rm c}$Hardy). During each visit, measurements were made in X-rays (0.3–10 keV) as well as six UV/optical bands: UVW2, UVM2, UVW1, *U*, *B*, and *V* (see Fig. 1). The data were reduced using tools included in HEASOFT (HEASARC 2014); the procedure is described in R. Edelson et al. (2015).

In addition to the X-ray light curve, we obtained a time-averaged *Swift*-XRT spectrum covering the period 2021 February 7 to May 6 (MJD 59252–59340 inclusive) using the online *Swift* data products generator[2] (P. A. Evans et al. 2009). The deadtime-

---

[2] https://www.swift.ac.uk/user_objects/

Table 1. Summary of observations made during the *Swift* intensive monitoring period.

Observatory	Filter	First obs. (MJD)	Last obs. (MJD)	$N_{\rm obs}$	Cadence (d)
Swift	X-ray	2021 Feb 7 (59252)	2021 May 6 (59340)	259	0.34
Swift	UVW2	‘	‘	218	0.41
Swift	UVM2	‘	‘	202	0.44
Swift	UVW1	‘	‘	192	0.46
Swift	U	‘	‘	194	0.45
Swift	B	‘	‘	216	0.41
Swift	V	‘	‘	238	0.37
LCO + Zowada	u	2021 Feb 8 (59253)	2021 Apr 21 (59325)	83	0.87
LCO + Zowada	g	2021 Feb 7 (59252)	2021 May 2 (59336)	91	0.92
LCO + Zowada	r	‘	2021 May 1 (59335)	87	0.95
LCO + Zowada	i	‘	‘	89	0.93
LCO + Zowada	z	‘	2021 Apr 23 (59327)	83	0.90

corrected on-source time is 215 ks and the spectrum contains 114 070 counts in the 0.3–10 keV range.

2.1.2 *Las Cumbres Observatory*

The LCO (T. M. Brown et al. 2013) is a network of 25 small (0.4–2 m) telescopes located at seven sites around the globe. MCG +08–11–11 has been monitored by the LCO with 4 d cadence since 2020 January, with the cadence intensifying to 1 d during the intensive *Swift* campaign. Sinistro cameras on the LCO 1-m telescopes were used on each visit to take a pair of CCD images per filter, enabling internal consistency checks for statistical errors and facilitating the identification of outliers due to cosmic ray hits or other anomalies. Exposure times were 120 s in the u band, 30 s in the B, g, V, r, and i bands, and 60 s in z_s, typically yielding photometric uncertainties of approximately 1 per cent, as estimated from the light curves of comparison stars. The reduced CCD images were obtained from the LCO Archive,[3] having undergone standard bias subtraction and flat-field correction. Photometric measurements were extracted using the AGN Variability Archive (AVA) pipeline.[4] Detailed procedures for photometric extraction and absolute calibration are described in J. V. Hernández Santisteban et al. (2020). In summary, aperture photometry was carried out using SEXTRACTOR (E. Bertin & S. Arnouts 1996), with a 5 arcsec radius aperture chosen to balance signal-to-noise ratio (S/N) and seeing variations across the monitoring campaign. Zero-points for individual images were determined by cross-matching field stars with the APASS catalogue (A. A. Henden et al. 2018) and PAN-STARRS (for z_s H. A. Flewelling et al. 2020). A bootstrapping simulation was employed to estimate the zero-point and its associated 1σ uncertainty. These zero-point corrections were applied to all light curves prior to the intercalibration described below.

2.1.3 *Dan Zowada Memorial Observatory*

The Dan Zowada Memorial Observatory (hereafter Zowada: R. Carr et al. 2022) is a fully robotic 0.5 m telescope operated by Wayne State University and which, at the time of this campaign, was situated in New Mexico, USA. It is capable of providing photometery in the Sloan bands u', g', r', and i' (M. Fukugita et al. 1996) and the Pan-STARRS z_s band (J. L. Tonry et al. 2012); hereafter we simply refer to these bands as u, g, r, i, and z. Zowada monitored MCG +08–11–11 with approximately daily cadence between 2020 September and 2021 April, overlapping with the intensive *Swift* monitoring mentioned above. The exposure times were 300 s, with two exposures per visit in g, r, and i, three in z, and four in u.

The data reduction pipeline is described in R. Carr et al. (2022). Differential aperture photometry was performed following the procedure outlined in J. A. Miller et al. (2023, 2025). Briefly, photometry was performed using a circular source aperture with radius 5 pixels, and a background annulus with inner and outer radius of 20 and 30 pixels. The total flux from three comparison stars was assumed to be constant over time in order to determine the light curve of the AGN in each band. Given the high cadence of the observations from each facility during our campaign (Table 1), we were able to flux-calibrate the Zowada light curves with respect to the LCO ones in each matching filter. This involved preforming a simple linear interpolation on to a common series of times, then determining the flux offset and scaling factor to be applied to the (normalized) Zowada light curves in order to bring them into agreement with the LCO ones (in mJy). Having then converted the Zowada light curves to mJy, the LCO and Zowada light curves were merged. The resulting combined optical–infrared light curves are shown in Fig. 2.

2.2 Archival observations

2.2.1 NuSTAR

A 25 ks hard X-ray observation of MCG +08–11–11 was made by the *Nuclear Spectroscopic Telescope Array* (*NuSTAR*; F. A. Harrison et al. 2013) on 2021 December 18 (observation ID: 90701640002), approximately 7 months after the conclusion of our intensive *Swift* monitoring period. These data were originally obtained for a study of the X-ray and mm intraday variability of MCG +08–11–11 by P. O. Petrucci et al. (2023). We reduced these data with up-to-date software (NUSTAR DATA ANALYSIS SOFTWARE v2.1.1) and calibration files (CALDB version 20210315). The source spectra for each focal plane module (FPMA and FPMB) were extracted from circular regions of radius 60 arcsec centred on the source. The background spectra were extracted from 120 arcsec-radius regions away from the source. The net 3–50 keV source count rates were 1.047 ± 0.007 and 0.967 ± 0.006

---

[3] http://archive.lco.global

[4] http://alymantara.com/ava

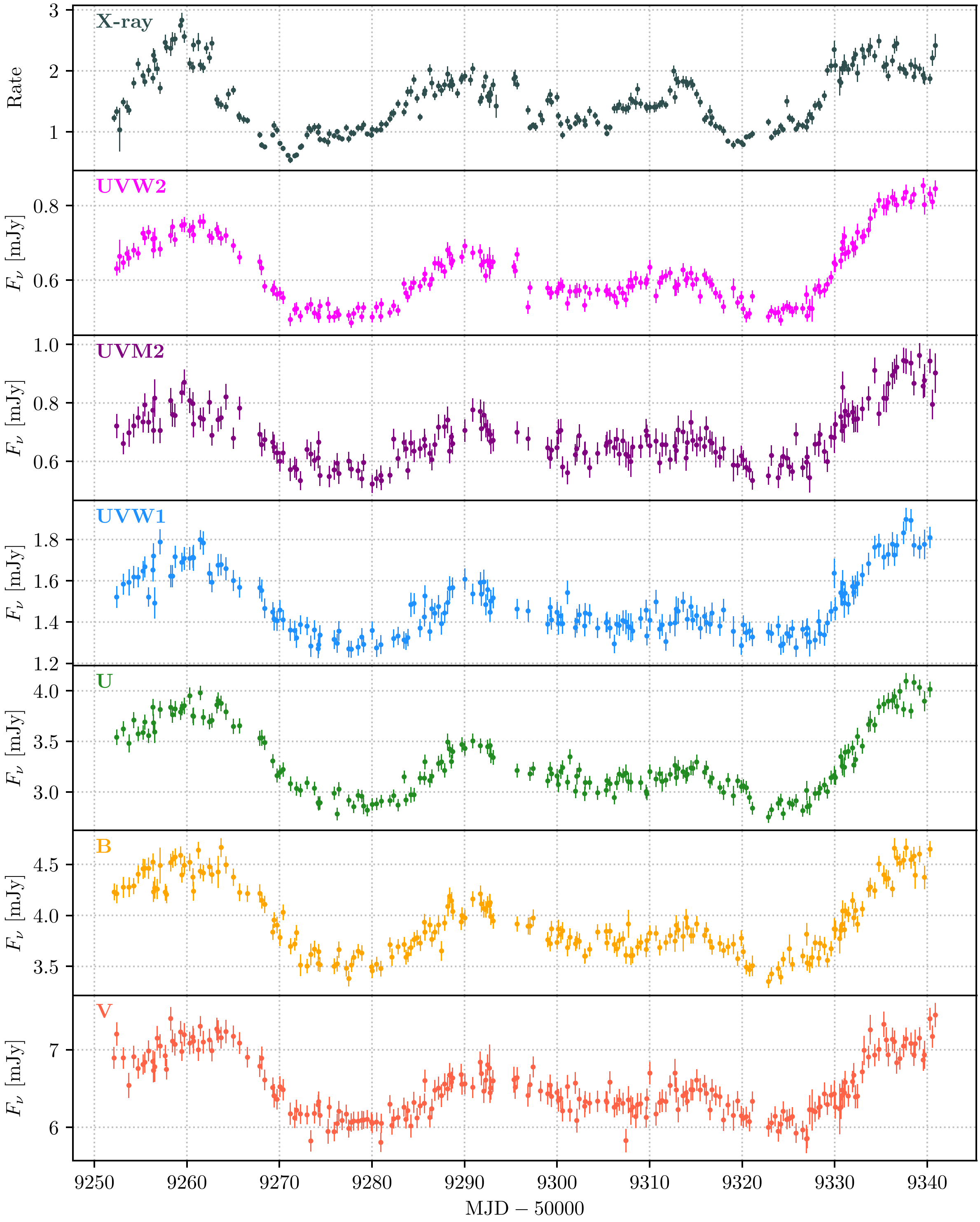

Figure 1. *Swift* XRT (top panel) and UVOT (lower panels) light curves from the 3-month period between 2021 February 5 and May 7.

counts s^{-1} in FPMA and FPMB, respectively. We model these spectra in Section 4.1.

2.2.2 XMM–Newton

A 38 ks X-ray observation of MCG +08–11–11 was made by the *XMM–Newton* Observatory (F. Jansen et al. 2001) on 2004 April 10 (observation ID: 0201930201). G. Matt et al. (2006) reported ≈ 10 per cent X-ray flux variations and no spectral variations during the observation. The authors then modelled the time-averaged EPIC-pn spectrum with a power-law continuum plus Compton reflection model. They found a relatively hard continuum spectrum, $\Gamma \approx 1.8$, and substantial soft X-ray absorption by both neutral ($N_{\mathrm{H}} = 1.8 \times 10^{21}$ cm^{-2}) and ionized ($N_{\mathrm{H}} = 1.1 \times 10^{22}$ cm^{-2})

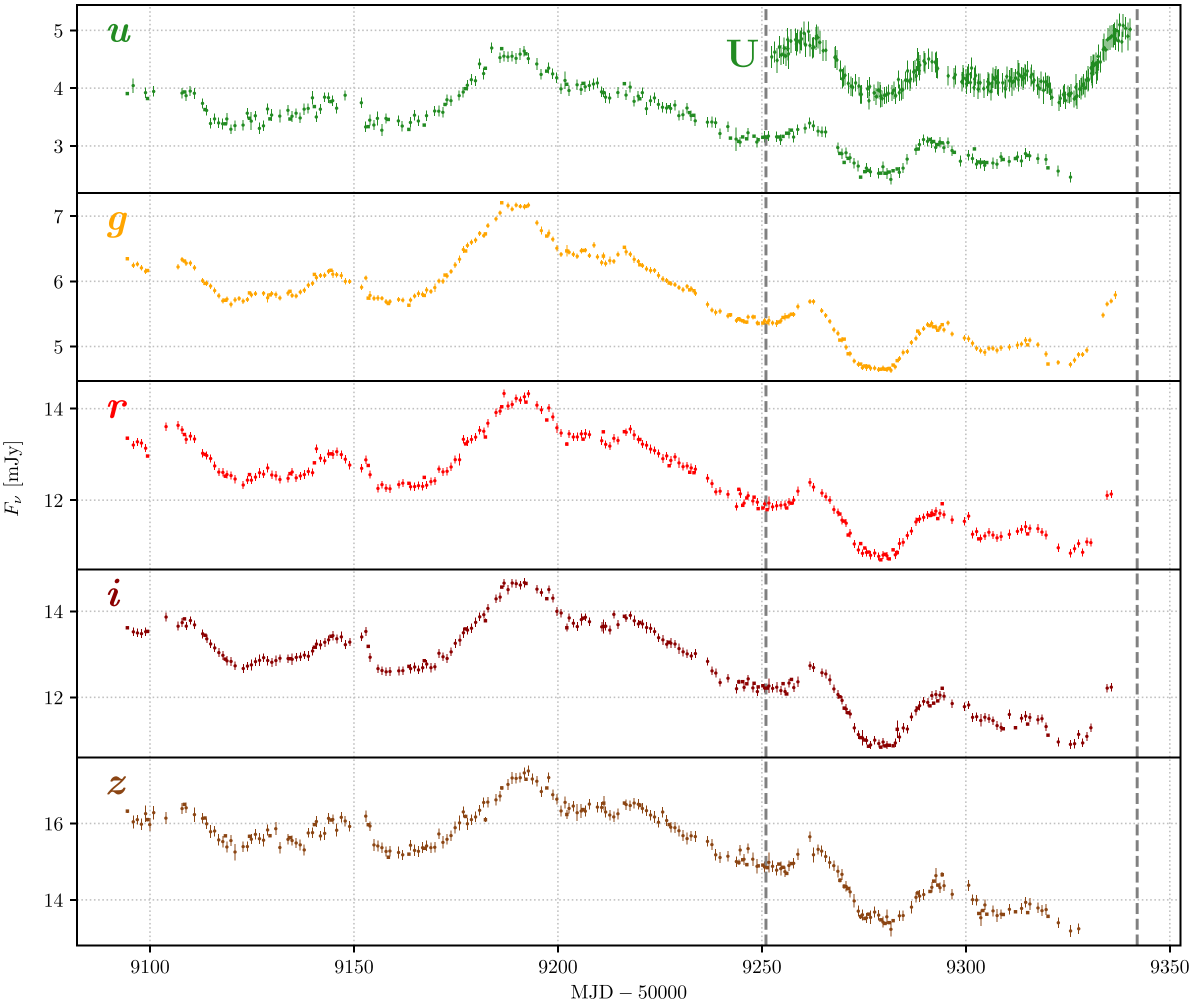

Figure 2. The combined Zowada and LCO light curves from the 8 months between 2020 September and 2021 May. The beginning and end of the intensive 3-month *Swift* monitoring period are indicated by vertical grey dashed lines. The *Swift* UVOT *U*-band light curve is shown in the top panel (offset by 1 mJy) for comparison.

gas within MCG +08–11–11. No excess soft X-ray emission above the power-law continuum was detected, and relativistic broadening of the Fe Kα fluorescence line was ruled out. We employ these archival data in Section 4.2.

3 TIMING ANALYSES

As can be seen by eye in Figs 1 and 2, substantial flux variability can be seen in all of the light curves. The light curves are clearly correlated, and the same variability patterns are apparent at all wavelengths. We therefore perform timing analyses to characterize the observed variability, assess the degree of correlation, and determine the wavelength dependence of time lags between the different bands.

These timing analyses will provide empirical links between the observed multiband light curves. By quantifying the variability amplitudes, inter-band correlations, and wavelength-dependent delays, we can later test whether the observed behaviour is consistent with a pure disc or BLR reprocessing (if either). The resulting parameters form the basis for the physical interpretation developed in Sections 4 and 5.

3.1 Flux–flux analysis and fractional variability

In this subsection we separate the variable AGN emission from the constant host-galaxy light so that we can more accurately determine the strength of the reverberation signal.

3.1.1 Flux–flux analysis and AGN/host galaxy decomposition

In order to separate the variable and constant components within the light curves, we fit the multiband flux densities ($F_\nu[\lambda, t]$ in mJy) as a function of wavelength and time in the form

$$F_\nu(\lambda, t) = A_\nu(\lambda) + S_\nu(\lambda)\mathrm{X}(t), \quad (1)$$

where $\mathrm{X}(t)$ is a dimensionless light curve scaled such that $\langle \mathrm{X} \rangle = 0$ and $\langle \mathrm{X}^2 \rangle = 1$; $A_\nu(\lambda)$ represents the mean spectrum, i.e. $F_\nu(\lambda, t)$ when $\mathrm{X}(t) = 0$; and $S_\nu(\lambda)$ is the rms spectrum, i.e. the variable component. An iterative decomposition procedure is used to determine $A_\nu(\lambda)$ and $S_\nu(\lambda)$, as described in Appendix A.

The results of this flux–flux analysis are shown in Fig. 3, and the values are given in Appendix A (Table A1). The linear flux–flux relations for each photometric band (the left-hand panel of Fig. 3) indicate that there is little or no colour change in the

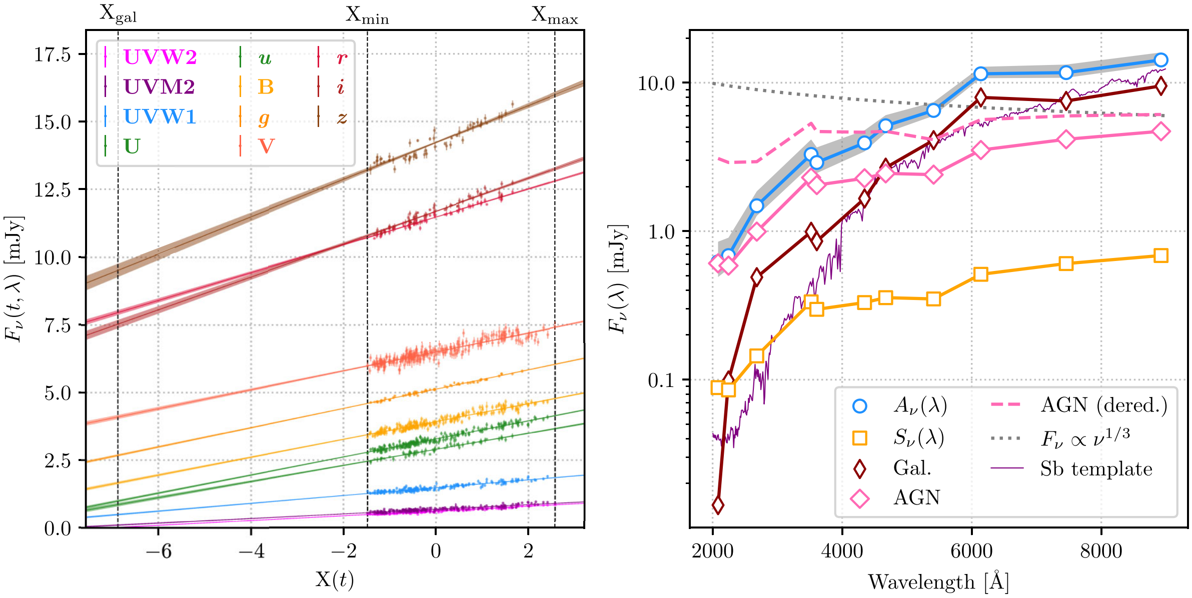

Figure 3. lux–flux analysis of the *Swift* UVOT, LCO and Zowada data, used to separate the variable and constant components of the light curves. The left-hand panel shows the observed flux densities against a dimensionless light curve shape X(t), which is normalized to mean 0 and rms 1. A linear regression extrapolates the flux–flux relations back to X$_{\rm gal}$, at which point the variable component is zero and the values of $F_\nu(\lambda, t)$ give the spectrum of the constant, host galaxy, component. The right-hand panel shows the galaxy component as a the deep red line and thin open diamonds. (The thin purple line shows the template spectrum of a barred spiral 'Sb' galaxy, reddened for comparison with the other observed spectra.) The right-hand panel also shows the average SED, $A_\nu(\lambda)$, i.e. $F_\nu(\lambda, t)$ where $\mathrm{X}(t) = 0$, as a blue line with open circles. The grey envelope, evaluating the linear model at X$_{\rm max}$ and X$_{\rm min}$, shows the AGN flux range seen during the campaign. The difference between the average SED, $A_\nu(\lambda)$, and the galaxy component represents the average spectrum of the observed variable AGN component, shown as a solid pink line and wide pink diamonds. The dashed pink line shows the average AGN component corrected for Galactic reddening ($A_{\rm V} = 0.568$ mag). The rms of the variable AGN component, $S_\nu(\lambda)$, is shown as an orange line with open squares. The dotted grey line shows a canonical optical accretion disc spectrum with $F_\nu \propto \nu^{1/3}$ scaled to match the dereddened AGN spectrum in the IR.

variable component as it brightens and fades. A simple model combining a variable flux component plus a constant flux component, both of fixed spectral shape, is therefore a reasonable representation of the observations.

The values of $F_\nu(\lambda, t)$ in the different wavebands, extrapolated back to where $F_\nu(\lambda, t)$ is 1σ above zero in the bluest waveband (UVW2), provide the SED of the constant, host galaxy, component. The difference between the mean overall spectrum, $A_\nu(\lambda)$, and the host galaxy gives the mean spectrum of the variable AGN component. These spectra are shown in the right-hand panel of Fig. 3. We see that, as expected, the AGN component is bluer than the galaxy component. The total spectrum is dominated by the host galaxy longward of the g band (≈ 4500 Å) but by the AGN at shorter wavelengths. In Fig. 3 we also show the template spectrum of a barred spiral galaxy (appropriate for MCG +08–11–11: G. de Vaucouleurs et al. 1991) taken from the SWIRE template library (M. Polletta et al. 2007). Our flux–flux derived galaxy spectrum matches the template reasonably well in the optical–infrared but less so in the ultraviolet, in which the template is generally redder (although the differences are exaggerated by the logarithmic scale of the plot). The bluest point (UVW2) of the galaxy spectrum lies below the template since, by construction, we assume the galaxy flux here is near zero (see Appendix A). The shape and scale of the blue end of the spectrum clearly depend on the choice of where to set X$_{\rm gal}$. It is also possible that the flux–flux procedure does not produce a precisely correct spectral decomposition, a point we return to in Section 6. Similar to what we see here, R. Prince et al. (2025) also find that their flux–flux galaxy spectrum is a poorer fit in the ultraviolet to a template selected for NGC 7469.

Having estimated the constant host galaxy spectrum, we can now assess the variability of the AGN emission in isolation.

3.1.2 *Fractional variability*

We calculate the relative amount of variability in each band, both in the raw and host galaxy subtracted light curves, informed by the results from our flux–flux analysis above. The fractional variability $F_{\rm var}$ is defined in the standard way: given a set of fluxes f with uncertainties σ_f and variance S^2,

$$F_{\rm var} = \sqrt{\frac{S^2 - \langle \sigma_f^2 \rangle}{\langle f \rangle^2}} \tag{2}$$

and the associated uncertainty is calculated following S. Vaughan et al. (2003). We calculate $F_{\rm var}$ for both the raw light curves and again after subtracting the (constant) host galaxy flux, as determined above. Both sets of $F_{\rm var}$ values are listed in Table 2. As expected, the fractional variability in X-rays (≈ 0.32) is much greater than that in the UVOIR bands ($\lesssim 0.15$). When measuring $F_{\rm var}$ of the raw light curves, there is a pronounced drop in variability with increasing wavelength up to the r band, beyond which we find the i and z bands have similar $F_{\rm var}$ to r (≈ 0.04). This decrease in the fractional variability is likely due to the dilution by the (constant) host galaxy flux, which has an increasing contribution at longer wavelengths. Subtracting the flux–

Table 2. X-ray, UV, optical, and infrared fractional variabilities, and inter-band correlations and observed-frame lags.

(1) Filter	(2) λ_{eff} (Å)	(3) F_{var}	(4) F_{var} gal. sub.	(5) r_{max}	(6) CCCD lag (d)	(7) CCPD lag (d)	(8) JAVELIN lag (d)
X-ray	–	0.317 ± 0.004	–	0.85	-1.8 ± 0.2	$-1.8^{+0.8}_{-0.2}$	$-1.7^{+0.2}_{-0.3}$
UVW2	2083.95	0.142 ± 0.002	0.143 ± 0.002	–	–	–	–
UVM2	2245.03	0.127 ± 0.004	0.131 ± 0.004	0.92	$+0.1^{+0.3}_{-0.4}$	-0.1 ± 0.4	$+0.1 \pm 0.2$
UVW1	2681.67	0.094 ± 0.003	0.102 ± 0.003	0.94	$+0.6^{+0.3}_{-0.2}$	$+0.5^{+0.6}_{-0.7}$	$+0.7 \pm 0.2$
U	3520.88	0.100 ± 0.002	0.114 ± 0.002	0.95	$+1.2 \pm 0.2$	$+1.1^{+0.4}_{-0.5}$	$+1.3 \pm 0.1$
u	3608.04	0.082 ± 0.003	0.114 ± 0.005	0.95	$+1.4 \pm 0.3$	$+1.3^{+0.4}_{-0.7}$	$+1.3^{+0.1}_{-0.2}$
B	4345.28	0.082 ± 0.001	0.112 ± 0.002	0.92	$+1.2 \pm 0.2$	$+1.2 \pm 0.5$	$+1.4 \pm 0.2$
g	4671.78	0.060 ± 0.001	0.127 ± 0.002	0.96	$+1.2 \pm 0.2$	$+1.2^{+0.4}_{-0.3}$	$+1.2 \pm 0.1$
V	5411.45	0.054 ± 0.001	0.139 ± 0.004	0.90	$+1.6 \pm 0.2$	$+1.5^{+0.8}_{-0.6}$	$+1.8 \pm 0.2$
r	6141.12	0.037 ± 0.001	0.121 ± 0.004	0.96	$+2.3 \pm 0.3$	$+2.3^{+0.3}_{-0.4}$	$+2.4 \pm 0.1$
i	7457.89	0.043 ± 0.001	0.119 ± 0.004	0.95	$+2.6 \pm 0.3$	$+2.5 \pm 0.3$	$+2.6^{+0.1}_{-0.2}$
z	8922.78	0.041 ± 0.001	0.118 ± 0.006	0.92	$+2.9 \pm 0.4$	$+2.6^{+0.4}_{-0.6}$	$+2.7^{+0.4}_{-0.1}$

Note. All values relate to the 3-month period of intensive *Swift* monitoring (2021 February–May). The correlation coefficient and lags are measured with respect to the *Swift* UVW2 band. *Columns:* (1) photometric filter; (2) effective wavelength of the photometric filter; (3) fractional variability of the raw light curve; (3) fractional variability of the host galaxy flux subtracted light curve; (5) maximum correlation coefficient; (6) CCCD lag; (7) CCPD lag; (8) the lag determined by JAVELIN.

flux model host galaxy fluxes obviously makes little difference in the UV bands, but results in fairly constant F_{var} across the optical and infrared bands (≈ 0.12), with an excess in the g and V bands around 5000 Å. Additionally, we note that in the 6 months preceding the intensive *Swift* monitoring period the mean, host galaxy subtracted fluxes in the optical–infrared bands were $\approx$ 42 per cent greater and, during this period, the fractional variability of the light curves decreases progressively with wavelength from 0.131 ± 0.03 in u to 0.082 ± 0.003 in z.

Overall, the flux–flux analysis confirms that the variable component is nearly colour-independent. After subtracting the host galaxy contribution to the light curves, the intrinsic AGN fractional variability remains roughly constant across the UVOIR range.

3.2 ICCF interband lags

Having characterized the variability amplitudes, we next measure temporal relationships between the bands to determine any correlations and time delays between variations. We first calculate the cross-correlations and lags between our light curves using the interpolated cross-correlation function (ICCF) method described by B. M. Peterson et al. (1998) (we use a Python implementation of that routine: PyCCF;[5] M. Sun, C. J. Grier & B. M. Peterson 2018). The method creates many Monte Carlo simulations of the data; in each realization a random subset of the data points are selected (‘random subset selection’: RSS, estimating the uncertainty on the results due to sampling) and each data point has its flux modified by random noise on the scale of the flux uncertainty (‘flux randomization’: FR, estimating the uncertainty on the results due to flux errors). The centroid (above 80 per cent of peak correlation) and peak of each simulated ICCF is recorded and the lag (and its uncertainty) is then calculated from the location (and width) of both the cross-correlation centroid distribution (CCCD) and the cross-correlation peak distribution (CCPD). Generally, lag measurements from the CCCD are preferred (B. M. Peterson et al. 1998).

We used the *Swift* UVW2 band as the reference light curve[6] and, using an interpolation time step of 0.1 d and 10^4 Monte Carlo iterations, we searched for lags in the range ± 30 d. We find a strong correlation between the X-ray and UVW2 light curves ($r_{\mathrm{max}} = 0.85$) and very strong correlations between UVW2 and the longer-wavelength light curves ($r_{\mathrm{max}} \geqslant 0.90$). Both the CCCD and the CCPD indicate an X-ray lag of ≈ -1.8 d (i.e. variations in the X-ray light curve lead variations in the UV by ≈ 1.8 d). Lags for the longer wavelength bands are all positive (or are consistent with zero) and generally increase with wavelength up to ≈ 3 d for the z band. The full results are recorded in Table 2 and the ICCFs and CCCDs are shown in Fig. 4.

In summary, we measure strong correlations between all light curves and find a clear increase of lag with wavelength, with the X-rays leading the UV by ≈ 1.8 d and the z-band by ≈ 5 d, consistent with progressively larger reprocessing radii at longer wavelengths.

3.3 JAVELIN interband lags

To verify the ICCF results and obtain statistically robust uncertainties on the lag measurements, we repeated the lag analysis using the model-based JAVELIN approach (Y. Zu et al. 2016). JAVELIN assumes that the AGN variability can be approximated by a damped, random walk (DRW). It creates a statistical model of the specfied driving light curve and uses this as a prior to model each lagged light curve, assuming that each is a smoothed, scaled, and time-shifted version of it. In the following text, we have used version 0.35 of JAVELIN in spectroscopic RM mode. In this mode, JAVELIN fits for the scale and amplitude of the DRW

---

[5] http://ascl.net/code/v/1868

[6] This was the natural choice because it is the shortest-wavelength UVOIR light curve and has the highest S/N (Fig. 1). It also makes comparisons with the JAVELIN analysis easier, since – because of the assumptions made in its modelling – JAVELIN requires the leading (or ‘driving’) light curve to be input as the reference, and we expect variations at shorter wavelengths to lead those at longer wavelengths.

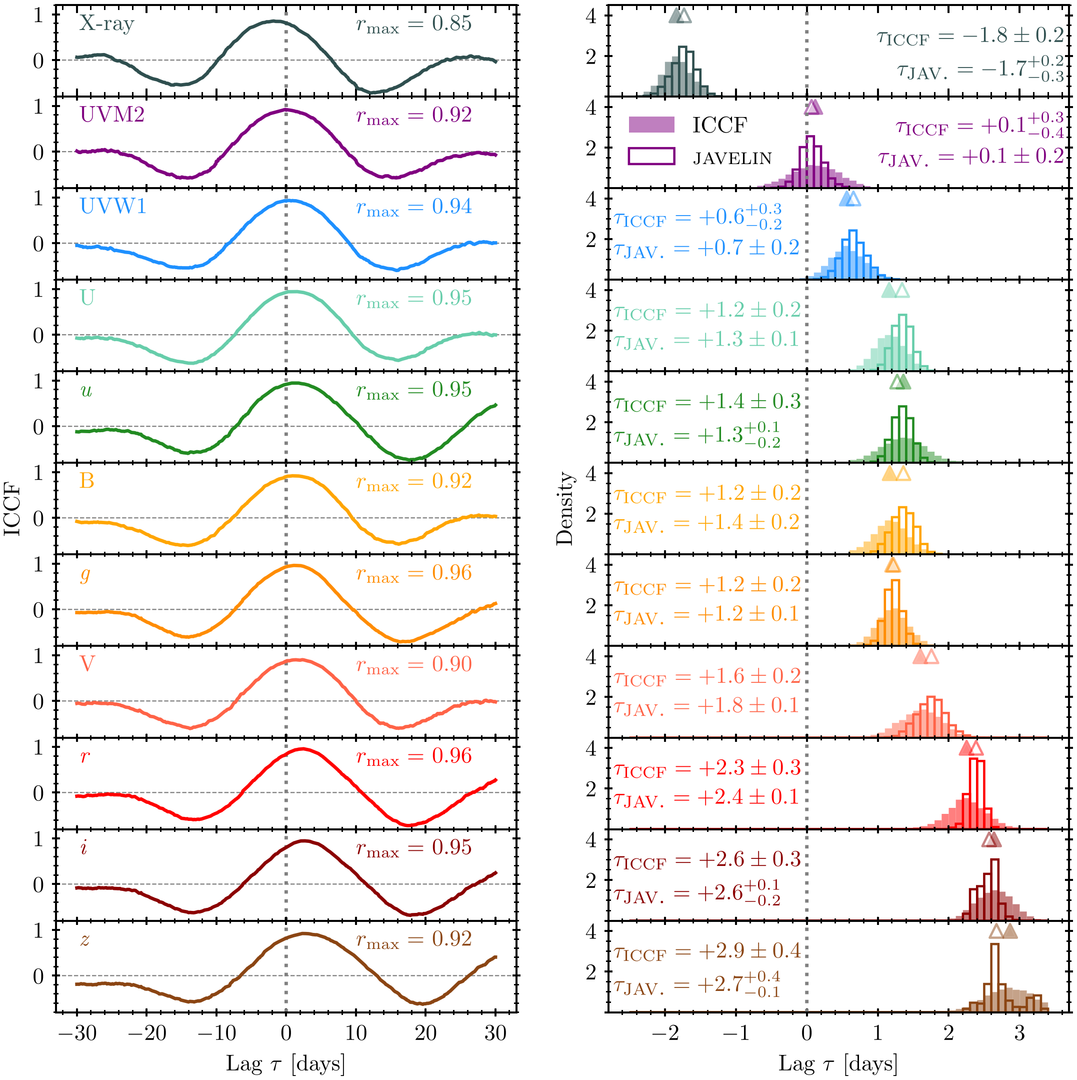

Figure 4. Results from the time series analyses of the MCG +08–11–11 intensive continuum RM campaign. All measurements are relative to the *Swift* UVW2 band (2084 Å). The left-hand panels show the ICCFs, with their maxima $r_{\max}$ given in the inset text. The corresponding right-hand panels contain the CCCDs, shown as solid histograms. Also shown are the JAVELIN-derived lag distributions (open histograms). The filled and open triangles indicate the centroid lag τ for the ICCF and JAVELIN methods, respectively; the inset text quotes each lag and its uncertainty.

model (determined from the driving light curve) and then for the lag, scale, and the width of the smoothing function for each longer wavelength light curve.

To determine the X-ray lead, we input the X-ray light curve as the driving light curve for the UVW2 band. For all other measurments, we have used the UVW2 light curve as the driving light curve, as was the case for the ICCF analysis. Informed by the ICCF analysis (Section 3.2), we searched for lags in a narrower range (±5 d). Since we expect the smoothing to be of the order of the lag, we also restricted the width of the smoothing top-hat function to < 5 d.

The JAVELIN lags are reported in Table 2, and the lag distributions derived from its MCMC sampling are shown as open histograms in Fig. 4. The JAVELIN lags are in very good agreement with the ICCF ones, again revealing an X-ray lead of ≈ 1.7 d and lags relative to UVW2 increasing with wavelength up to ≈ 3 d in the near-infrared z band. In the UVOIR bands, the JAVELIN lag uncertainties are smaller than the corresponding ones determined by the ICCF method, which can be seen by eye in Fig. 4. These smaller uncertainties are expected, since tests performed on simulated light curves have demonstrated that JAVELIN produces lower and more accurate error estimates than the ICCF method (e.g. J. Li et al. 2019, Z. Yu et al. 2020), provided that the simplest underlying assumptions of reverberation are valid. Additionally, since we adopted the RSS procedure in calculating the ICCF lags (which is not essential for well-sampled light curves such as ours) the associated uncertainties will be increased as a result of not using the full data sets.

The close agreement between JAVELIN and ICCF lags reinforces that the observed correlations relate to genuine reverberation delays rather than artefacts of the sampling. We discuss this further in Appendix B.

3.4 Reanalysis of the 2019–20 Wise Observatory light curves

In the preceding subsections we determined the X-ray to IR lag spectrum from the light curves obtained during our intensive

7*Swift* monitoring campaign. Because a prior campaign reported much longer optical lags, we revisit those data to test whether the differences reflect sampling effects or physical changes. The lags we have determined for the intensive *Swift* monitoring period are much shorter than those recently reported by C. Fian et al. (2023) following an optical photometric monitoring campaign on MCG +08–11–11 conducted between 2019 October and 2020 April using the C18 telescope at the Wise Observatory in Israel. These observations span a period between 16 and 10 months prior to the beginning of our intensive *Swift* monitoring. The Wise-C18 observations were made with approximately nightly cadence in five narrow optical bands (centred on 4250, 5700, 6200, 7320, and 8250 Å), chosen to sample the optical AGN continuum emission and avoiding broad emission lines. Fig. 5 shows that the optical variability in the earlier campaign is different in character to that seen during our *Swift* monitoring period. The Wise light curves show mainly a slow (∼months) smooth rise and subsequent fall in brightness. In contrast our *Swift* light curves (Fig. 1) exhibit more prominent faster variability (over ∼days–weeks). We also note that the mean optical flux during the earlier campaign is approximately a factor of 4 higher than that we observed: C. Fian et al. (2023) report $\langle F_{4250\,\text{Å}} \rangle = 8.48$ mJy, compared with $\langle F_{\rm B} \rangle = 2.27$ mJy during the intensive *Swift* monitoring period.[7] C. Fian et al. (2023) employed several different methods to determine the optical interband lags and found that the mean lag of the 8250 Å band relative to 4250 Å was 7.1 ± 1.1 d. From Fig. 6 it can be seen that the lag between these wavelengths is only ≈ 1.6 d in our data.

We have reanalysed the optical light curves of C. Fian et al. (2023) using the ICCF method and JAVELIN and confirm their lag determinations and very steep lag spectrum. In some previous monitoring observations it has been found that the presence of short lags can be obscured if there are also longer term trends in the light curves (W. F. Welsh 1999; I. M. M$^{\rm c}$Hardy et al. 2014; M. Pahari et al. 2020). Removal of such trends can reveal the shorter lags. Here we fitted the long-term trends in the light curves using a Locally Weighted Scatterplot Smoothing (LOWESS) filter with a width of ≈ 45 d. This fit results in smoothed optical light curves that contain the variability on ≈month time-scales. Subtracting the smoothed light curves from the observed ones leaves behind just the faster variability (Fig. 5). We then determined the lags between these filtered light curves using both the ICCF method and JAVELIN. The results of these tests are contained in Table 3. The lags between the filtered light curves are much shorter than those reported by C. Fian et al. (2023) and (as shown in Fig. 6) are entirely consistent with our own lags from the 2021 data set.

In Appendix C we further investigate the effects of detrending the light curves on the recovered lags. We conclude that the shorter lags determined following the detrending procedure do not result simply from the removal of the low-frequency components of a single broad response. Rather, it appears that the filtering distinguishes two separate components in the signal: a fast reprocessing component and slower large-amplitude trend of unknown origin (possibly resulting from slow-moving temperature fluctuations across the disc, e.g. J. M. M. Neustadt & C. S. Kochanek 2022). In summary, the earlier long lags were largely the result of slow large-amplitude trends in the light curves; shorter lags, consistent with our own, are retrievable in the earlier data following detrending. Having verified our lag measurements we next assemble a full lag spectrum and conduct a first pass at comparing it to a physical model.

3.5 Combined lags and preliminary modelling

We now combine all lag measurements from the above to construct a complete lag-versus-wavelength spectrum and make a first comparison with a simple standard accretion disc model. This will inform us how well our data conform to basic assumptions about the reverberation process and whether more detailed modelling is required. In Fig. 6 we present all the observed lags, relative to the *Swift* UVW2 band, derived using both ICCF (blue squares) and JAVELIN (red circles) for all of the *Swift*, LCO, and Zowada light curves from the season of intensive observation. We also present the JAVELIN lags from the de-trended Wise Observatory observations, with their zero-point being adjusted so that the 4250 Å -band has a lag of 1.36 d, which is the JAVELIN lag of the *Swift B* band (4345 Å) relative to UVW2. Because these bands are close in wavelength, further interpolation would alter the lag negligibly, and given the uncertainties around that wavelength, no further adjustment is warranted. These Wise lags are shown only for comparison and are not used in the subsequent modelling.

In Fig. 6 we show model lags calculated using the same numerical code used by I. M. M$^{\rm c}$Hardy et al. (2018) (based on illumination of an accretion disc with a temperature profile as described by N. I. Shakura & R. A. Sunyaev 1973) who compared the observed and model lags of five AGN. Here we take a mass of 2.82×10^7 M$_\odot$, an accretion rate of 20 per cent of Eddington (based on CREAM modelling of the optical light curves by M. M. Fausnaugh et al. 2018), an illuminating luminosity of 2.7×10^{44} erg s^{-1}, based on a factor of 2 extrapolation of the *Swift* BAT 14–195 keV observed luminosity (A. Y. Lien et al. 2025), an albedo of 0.2, and a lamppost source model with a height of 10 $R_{\rm g}$. These parameters are similar to those used by I. M. M$^{\rm c}$Hardy et al. (2018); small changes in source height or illuminating luminosity have little effect on the UV–optical lags. Neither that work nor the present model includes a colour-correction factor, which can influence the lag spectrum, although I. M. M$^{\rm c}$Hardy et al. (2023) found that NGC 4395 required almost none. We return to this point in more detailed modelling.

Predicted lags for a non-rotating Schwarzschild black hole (solid green line) and a maximally rotating Kerr black hole (dashed orange line) are shown in Fig. 6. They are calculated relative to the X-rays, rather than UVW2 as our data; however, for a source height of 10 $R_{\rm g}$, the resulting offset of 0.03 d is negligible.

I. M. M$^{\rm c}$Hardy et al. (2018) found that the ratio between the observed and model lags, between the UV and V bands, was between a factor of 1 and 2 for a non-rotating black hole. Looking broadly at the overall shape of the lag spectrum we find the same result here with a ratio of ~ 2.5. However, and again in agreement with I. M. M$^{\rm c}$Hardy et al. (2018), we find a larger discrepancy between the observed and model lags between the X-ray and UV bands.

In detail, however, we see that the observed lag spectra do not agree well with this simple model. Besides the discrepancy between the amplitude of the observed and model X-ray to UV lags, the curvature of the lag spectrum does not agree with the upwardly curving shape with increasing wavelength of $\tau \propto \lambda^{4/3}$ expected from simple disc reprocessing. In fact the gradient of the lag spectrum decreases with increasing wavelength, with the

---

[7] Both estimates of the flux density have had the host galaxy contribution subtracted. C. Fian et al. (2023) also note that their optical fluxes are also a factor 2 higher than those reported by M. M. Fausnaugh et al. (2017).

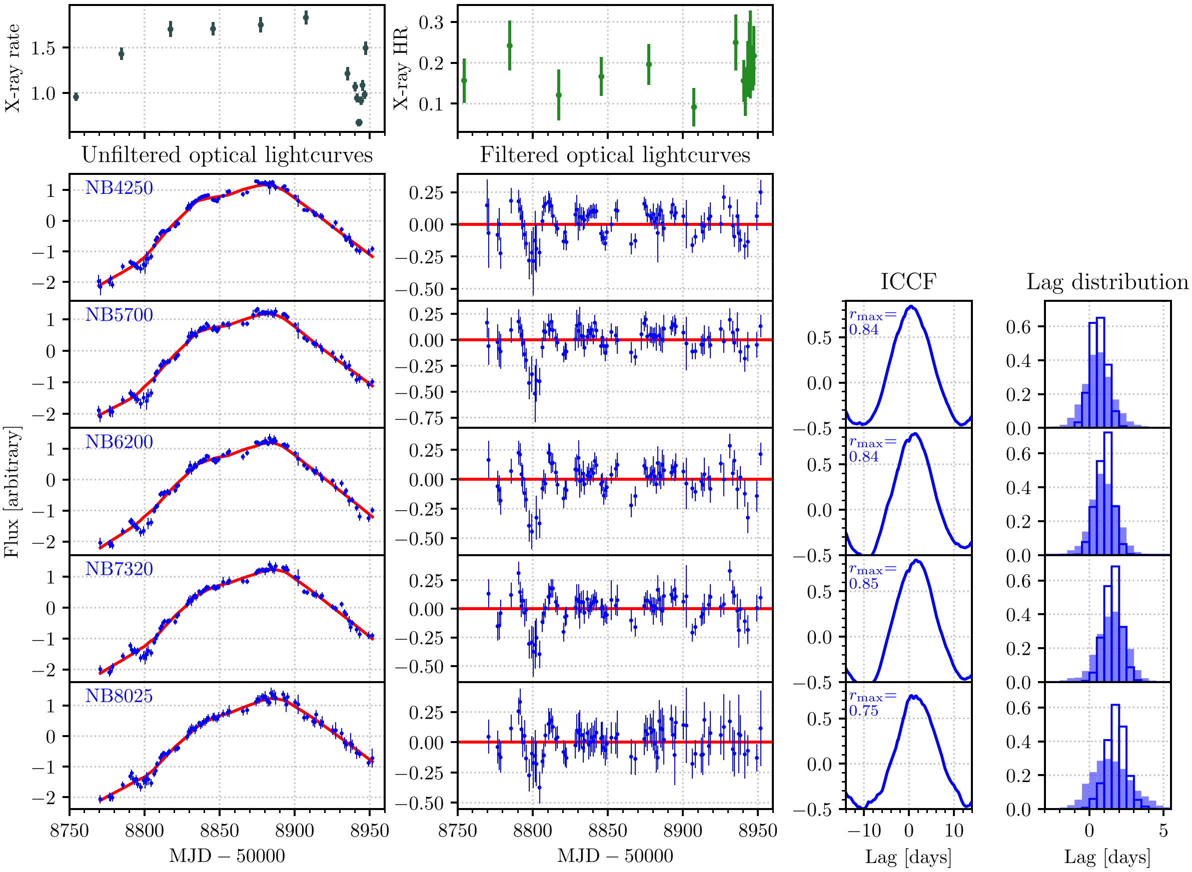

Figure 5. *Swift* X-ray and Wise Observatory narrow band optical light curves of MCG +08–11–11 in the period 2019 October to 2020 April. *Top*: the *Swift* XRT light curve (left) and hardness ratio (right; using 0.3–1.5 and 1.5–10 keV bands) are shown for comparison. *Left*: the original light curves presented by C. Fian et al. (2023) in which long-term trends (solid red lines) have been estimated using the LOWESS method with a 45 d smoothing window. (The optical fluxes have been normalized to have a mean of 0 and standard deviation of 1.) *Centre*: the filtered light curves, from which the long-term trend has been subtracted. *Right:* the ICCF and lag distribution for each filtered light curve relative to the 4250 Å band. The solid and open histograms show the ICCF centroid JAVELIN lag distributions, respectively.

lags approaching an asymptotic value. It is actually well described ($\chi^2 = 6.7$, d.o.f. $= 8$, $P = 57$ per cent using the ICCF centroid lags) by $\tau \propto \lambda^{0.5}$ over all observed wavebands. Although not exactly the same, a similar approach of the lags to an asymptotic value at long wavelength was seen in NGC 4395 (I. M. M$^{\rm c}$Hardy et al. 2023) and interpreted as an indication that there was an edge to the reprocessing region. In fact a decrease in the gradient of the model lag spectra can be seen at the very longest wavelengths as the model contains a disc edge at 4800 $R_{\rm g}$ at the dust sublimation temperature (here, 2000 K) on the surface of the disc.

However the most prominent features of the observed lag spectrum, which are not expected from disc reprocessing, are the two large bumps, where the lags are in excess of the lags in the surrounding bands, one centred around the *u* band and the other near the *i* band. These bumps are indicative of the Balmer and Paschen continua respectively, expected from reprocessing in the BLR (K. T. Korista & M. R. Goad 2001, 2019; H. Netzer 2020). These bumps have been seen previously (e.g. E. M. Cackett et al. 2018; H. Netzer 2022) but the present examples are perhaps the most prominent and clearest yet presented.

In summary, the combined lag spectrum follows a form roughly $\tau \propto \lambda^{0.5}$, flatter than the canonical $\tau \propto \lambda^{4/3}$. Additional complexity includes the excesses around the *u* and *r*–*i* bands that may be indicative of reprocessing of the driving continuum by the BLR. These features motivate more detailed physically informed modelling. In Section 5 we will examine the origin of this complex lag spectrum in more detail. In order to calculate the most accurate models, we require the best available estimates of physical parameters such as the Eddington accretion ratio ($\dot{m}_{\rm E}$) and the SED of the ionizing radiation, which we discuss in Section 4.

4 SED SHAPE AND DETERMINATION OF $\dot{m}_{\rm E}$ AND MASS

Having established the temporal behaviour in the preceding section, we now use our time-averaged and archival multi-wavelength data to analyse the spectra and broad-band SED of MCG +08–11–11 to determine important physical parameters, particularly its Eddington accretion ratio ($\dot{m}_{\rm E}$), and mass, parameters, which determine both the geometry and therefore the lag spectrum of the source.

4.1 The hard X-ray spectrum and $\dot{m}_{\rm E}$

The hard X-ray spectral index is an indicator of $\dot{m}_{\rm E}$ (e.g. A. Kubota & C. Done 2018), with harder spectra being associ-

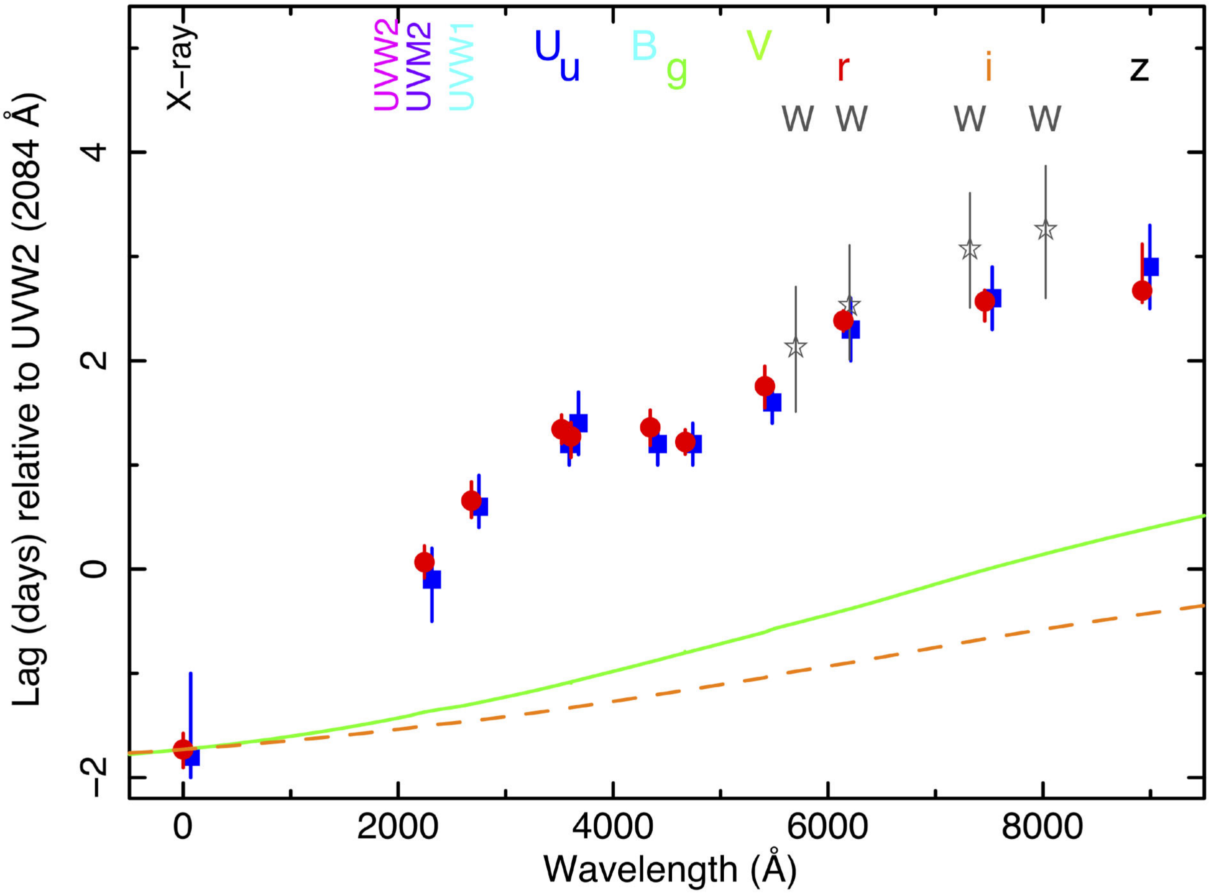

Figure 6. The lag spectrum of MCG +08–11–11 from the intensive *Swift* and LCO monitoring in 2021. All lags are measured relative to the *Swift* UVW2 band (2084 Å). The red filled circles are lags measured using JAVELIN and the blue filled squares are the ICCF centroid lags. The lag distributions for the individual bands are shown in Fig. 4. The solid green line is a simple numerical model fit to the lags expected from X-ray reprocessing from a disc around a non-rotating black hole of mass 2.82×10^7 M$_\odot$ and accretion rate of 20 per cent of Eddington. The dashed orange line is for reprocessing from a disc around a maximally rotating Kerr black hole. The open grey stars are the lags derived from the observations by C. Fian et al. (2023) at the Wise Observatory after filtering out long-term trends in the light curves.

Table 3. Optical band lags for the 2019–20 Wise Observatory data.

	Unfiltered			Filtered	
Filter	ICCF (centroid)	JAVELIN (spectro.)	JAVELIN (photo.)	ICCF (centroid)	JAVELIN (spectro.)
NB5700	$1.0^{+1.1}_{-1.0}$	1.3 ± 0.3	$2.2^{+1.6}_{-0.8}$	$0.55^{+0.98}_{-0.88}$	$0.77^{+0.58}_{-0.62}$
NB6200	$2.1^{+1.0}_{-1.1}$	2.7 ± 0.3	$2.8^{+0.8}_{-0.7}$	$0.96^{+0.83}_{-0.81}$	$1.17^{+0.58}_{-0.52}$
NB7320	$5.1^{+1.3}_{-0.8}$	3.8 ± 0.4	$4.1^{+0.7}_{-0.6}$	$1.54^{+0.90}_{-0.98}$	$1.71^{+0.54}_{-0.56}$
NB8025	$7.4^{+1.4}_{-1.1}$	5.3 ± 0.6	$7.3^{+1.5}_{-1.2}$	$1.44^{+1.41}_{-1.29}$	$1.90^{+0.61}_{-0.66}$

Note. All lags are measured relative to the narrow-band 4250 Å filter. The lags for the 'unfiltered' light curves were measured from the original data and were reported by C. Fian et al. (2023). The 'filtered' lags have been determined from the modified light curves, after removal of the long-term ($\sim$ 1 month) trends (see Section 3.4 in the text for details).

ated with lower accretion ratios. Here, we fit the time-averaged *Swift*-XRT spectrum from our campaign, together with the archival *NuSTAR* spectra recorded in 2021 December. To minimize the complications from absorption and emission-line features seen in previous observations, we fit only the 2–5.5 and 7.5–50 keV data with a simple power law for which we obtain a photon index $\Gamma = 1.697 \pm 0.008$ and $\chi^2_\nu = 1206/1121$ d.o.f = 1.08 (Fig. 7). The cross-normalization factors applied to the *NuSTAR* FPMA and FPMB spectra are similar at 0.96 ± 0.01 and 0.94 ± 0.01, respectively. We calculate the flux to be $\log(F_{2-10\mathrm{keV}}/\mathrm{erg\,s^{-1}\,cm^{-2}}) = -10.302 \pm 0.003$, corresponding to $L_{2-10\mathrm{keV}} = 4.79 \times 10^{43}\ \mathrm{erg\,s^{-1}} \approx 1.3$ per cent of the Eddington luminosity, assuming a mass 2.82×10^7 M$_\odot$ (M. M. Fausnaugh et al. 2017). Using the luminosity-dependent X-ray bolometric correc-

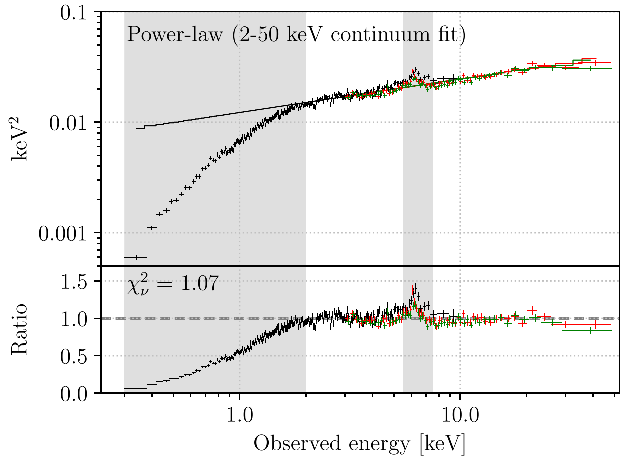

Figure 7. A power-law fit to the time-averaged *Swift*-XRT (black) and *NuSTAR* FPMA (red) and FPMB (green) spectra. Data in the shaded grey regions were excluded from the fit. The upper panel shows the unfolded spectrum and model. The lower panel shows the ratio of the data to the model.

tion of F. Duras et al. (2020), we estimate $\dot{m}_{\rm E} = L_{\rm bol}/L_{\rm Edd} \approx 0.23$. We return to this in Section 4.4 and Appendix D, where other multiwavelength indicators of $\dot{m}_{\rm E}$ are compared.

4.2 X-ray variability mass estimates

We next use the short-time-scale X-ray variability properties of MCG +08–11–11 to obtain an estimate of the black hole mass independent of optical reverberation-based methods. Black hole masses can be estimated from X-ray power spectral density (PSD) parameters, either from a bend in the PSD or from the normalization of the high-frequency part of the PSD (I. M$^{\rm c}$Hardy 1988; I. M. M$^{\rm c}$Hardy 2013). We compute the excess variance of the 38 ks *XMM–Newton* observation of G. Matt et al. (2006), binned at 250 s following G. Ponti et al. (2012), as 0.218 (counts s^{-1})^2 and a mean count rate of 15.09 counts s^{-1}, giving a normalized excess variance $\sigma^2_{\rm rms} = 9.57 \times 10^{-4}$. Using the 40 ks $\sigma^2_{\rm rms}$ –$M_{\rm BH}$ relation of G. Ponti et al. (2012) we obtain $M_{\rm BH} = 5.9^{+3.5}_{-1.8} \times 10^7$ M$_\odot$ (here the uncertainties in the mass are derived from the scatter in the relationship). This is more than twice the optical RM mass reported by M. M. Fausnaugh et al. (2017) but is consistent with that lower mass within the uncertainties.

We also combined the archival *XMM–Newton* light curve with that of our *Swift* campaign to construct a PSD spanning $\log(\nu/{\rm Hz}) = -7$ to -3, which we fit with a bending power-law using PSRESP (P. Uttley, I. M. M$^{\rm c}$Hardy & I. E. Papadakis 2002). Since we expect the slope below the PSD bend to be poorly determined by our observations we fix that slope to −0.8, similar to that found in better sampled observations (e.g. I. M. M$^{\rm c}$Hardy et al. 2004). The high-frequency slope is well constrained at −2.0 ± 0.5 (90 per cent confidence bounds), with no measurable bend at low frequencies. In an attempt to better localize the bend frequency we fixed the high-frequency slope at −2.0 and refit the PSD. The resulting fit is very good ($P = 0.93$) although no bend was found in the observed frequency range ($> 10^{-7}$ Hz). We searched for a bend in the range 10^{-9} to 10^{-5} Hz as a bend below the observed frequencies will have a flattening effect on the PSD in the lowest observable frequencies. The best-fitting bend frequency was almost at the limit of the frequencies searched (2.2×10^{-9} Hz) although the 90 per cent confidence region extends up to 1.5×10^{-6} Hz. We adopt the bolometric luminosity derived from $L_{5100\,\text{Å}}$ by M. M. Fausnaugh et al. (2017) and apply the I. M. M$^{\rm c}$Hardy et al. (2006) relation between PSD bend frequency, luminosity and mass, finding $M_{\rm BH} \sim 5$–70×10^7 M$_\odot$. (The lower end of this mass range relates to the upper uncertainty bound on the bend frequency and is consistent with the mass derived from the normalized excess variance.) We conclude that although the present X-ray data are not good enough to provide a precise measurement of the black hole mass, there are indications that the mass may be towards the upper limit of the range quoted by M. M. Fausnaugh et al. (2017), i.e. $\approx 8.3 \times 10^7$ M$_\odot$.

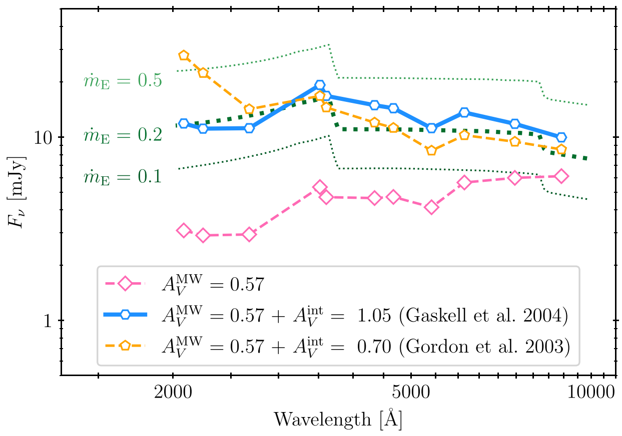

Figure 8. The green dotted lines show accretion disc + diffuse BLR continuum spectra for Eddington ratios $\dot{m}_{\rm E} = 0.1$, 0.2, and 0.5. The disc spectra are predicted by the model QSOSED and the diffuse BLR continua are scaled to these disc spectra according to K. T. Korista & M. R. Goad (2019). In pink diamonds we show the mean AGN spectrum from our flux–flux analysis, corrected only for Milky Way reddening $A_V^{\rm MW} = 0.57$ mag. The orange pentagons show the spectrum additionally corrected for intrinsic reddening with $A_V^{\rm int} = 0.70$ mag using the SMC Bar extinction curve of K. D. Gordon et al. (2003). The blue hexagons show the spectrum additionally corrected for intrinsic reddening with $A_V^{\rm int} = 1.05$ mag using the AGN extinction curve of C. M. Gaskell et al. (2004): this approximately matches the disc+BLR spectrum for $\dot{m}_{\rm E} = 0.2$.

Having now assessed both the spectral and timing properties of the X-ray data, we turn our attention to the UVOIR spectrum and overall SED to further refine our estimates of mass and $\dot{m}_{\rm E}$.

4.3 The UVOIR continuum: reddening and $\dot{m}_{\rm E}$

We next characterize the shape of the AGN UVOIR emission to estimate the intrinsic reddening within MCG +08–11–11, which, in turn, affects our estimate of $\dot{m}_{\rm E}$.

Fig. 8 shows in pink the AGN UVOIR spectrum output by the flux–flux analysis (Section 3.1) corrected only for Galactic reddening assuming the extinction curve of J. A. Cardelli et al. (1989) with $A_V = 0.568$ mag (E. F. Schlafly & D. P. Finkbeiner 2011). The observed spectrum is much redder than the expected $F_\nu \propto \nu^{1/3}$, suggesting either a cool disc or substantial intrinsic reddening. Strong X-ray extinction (e.g. G. Matt et al. 2006; S. Bianchi et al. 2010; A. R. Patrick et al. 2012) and UV resonance-line absorption are evidence of a substantial amount of gas within MCG +08–11–11 along our line of sight to the nucleus, so dust may also be present. G. W. Jaffarian & C. M. Gaskell (2020) estimated

$E(B-V) = 0.65$ mag from the optical Balmer decrement, further motivating our test of reddening here.

We compare the empirical UVOIR spectrum with model disc spectra for $\dot{m}_{\rm E} = 0.1$, 0.2, and 0.5 from QSOSED (A. Kubota & C. Done 2018), assuming the M. M. Fausnaugh et al. (2017) mass of 2.82×10^7 M$_\odot$ to which we have added a diffuse BLR component, appropriately scaled following K. T. Korista & M. R. Goad (2019). Rather than performing a formal fit, this was a simple heuristic exercise intended to identify plausible combinations of the intrinsic reddening and accretion rate. Dereddening the observed spectrum using two extinction curves (a 'flat' AGN curve from C. M. Gaskell et al. 2004 and the 'steep' SMC-Bar curve of K. D. Gordon et al. 2003), we find that the flat curve provides a reasonable match to the $\dot{m}_{\rm E} = 0.2$ disc+BLR model for $A_V^{\rm int} = 1.05$ mag, while the SMC curve overcorrects the UV flux (Fig. 8). Assuming the C. M. Gaskell et al. (2004) curve is appropriate, the dereddened UVOIR spectrum is consistent with $\dot{m}_{\rm E} \approx 0.20$, as implied by the X-ray spectrum. The flux correction factors for this curve and $A_V^{\rm int}$ are given in Table A1.

Next, in Section 4.4, we combine the UVOIR and X-ray spectra to produce an overall SED from which we make our best estimates of the mass, $\dot{m}_{\rm E}$, and reddening.

4.4 Broad-band SED modelling: mass, $\dot{m}_{\rm E}$, and reddening

With estimates of the intrinsic UVOIR and X-ray spectra in hand, we next attempt to obtain a self-consistent fit to the whole broad-band SED using the models QSOSED and AGNSED (A. Kubota & C. Done 2018). Our aim is to determine the combination of mass, $\dot{m}_{\rm E}$, and reddening, which best explain the overall SED.

We begin by assuming a non-spinning black hole with the mass fixed to the value 2.82×10^7 M$_\odot$ given by M. M. Fausnaugh et al. (2017). QSOSED assumes a stratified accretion flow geometry consisting of (i) a spherical hot corona around the black hole that produces hard X-rays; (ii) a warm Comptonizing inner disc that produces the soft X-ray excess emission; and (iii) a standard cold outer accretion disc from which the UVOIR spectrum arises (see fig. 2 of A. Kubota & C. Done 2018). In QSOSED some parameters, such as the accretion rate and X-ray spectral index, are physically linked. AGNSED assumes the same underlying geometry but is more flexible and some of the assumptions of QSOSED can be relaxed.

Fig. 9 shows the QSOSED model for $\dot{m}_{\rm E} = 0.2$ and $M_{\rm BH} = 2.82 \times 10^7$ M$_\odot$ (based on the analyses in Sections 4.1 and 4.3). This model matches the dereddened UVOIR spectrum (blue) but underpredicts the hard X-ray flux considerably, giving $\log(F_{2-10\,{\rm keV}}/{\rm erg\,s^{-1}\,cm^{-2}}) \approx -10.67$ and has a much softer X-ray spectrum that the observed one.

Using the more flexible model AGNSED we therefore perform a fit to only the hard X-ray continuum regions as in Section 4.1 and determine $\Gamma = 1.72$ (consistent with the simple power-law model), $\dot{m}_{\rm E} = 0.18$ and corona radius $R_{\rm hot} = 22.6$ $R_{\rm g}$. In neither our own preliminary X-ray analysis nor that of previous researchers (G. Matt et al. 2006; S. Bianchi et al. 2010; A. R. Patrick et al. 2012) has a soft X-ray excess been found. We therefore set the radius of the warm corona equal to that of the hot corona, so that no soft X-ray excess component was produced. The resultant model is shown by the solid black line in Fig. 9 and is a reasonable match to both the X-rays and the dereddened UVOIR spectrum.

Although the above AGNSED fit does match the X-ray spectral index, the accretion ratio has to be high to account for the X-ray luminosity, and this combination of spectral index and accretion ratio is not seen in the three AGN modelled by A. Kubota & C. Done (2018) or in the large sample studied by S. Hagen et al. (2024). It is not expected in the original QSOSED model where accretion ratio and X-ray spectral index are physically linked. The AGNSED fit also requires substantial reddening to reduce the expected UVOIR continuum to the observed levels. We therefore consider next the possibility that the observed UVOIR spectrum (corrected *only* for Galactic reddening, i.e. the pink line in Fig. 9) is actually the true source spectrum, and that it is not reddened by dust in MCG +08–11–11. This possibility requires a low $\dot{m}_{\rm E} \approx 0.03$. In the QSOSED model we also require a higher black hole mass (8.4×10^7 M$_\odot$) in order to produce the observed X-ray luminosity. This model does, however, produce a weak soft X-ray excess. A similar high-mass model with AGNSED, setting $R_{\rm warm} = R_{\rm hot}$, is also a reasonable match to the data with the hot inner corona extending to ≈ 120 $R_{\rm g}$, yielding little UV emission and no soft excess.

In summary, adopting the RM mass 2.82×10^7 M$_\odot$ implies that $\dot{m}_{\rm E} \approx 0.2$ (Appendix D) and requires substantial intrinsic reddening to explain the observed UVOIR spectrum. Alternatively, a higher mass ($\approx 8 \times 10^7$ M$_\odot$) and lower $\dot{m}_{\rm E} \approx 0.03$ can explain the faint red UVOIR spectrum without additional dust. This latter scenario may more naturally explain the slope of the hard X-ray spectrum, and the apparent lack of a soft X-ray excess, which A. Kubota & C. Done 2018 show disappears for $\dot{m}_{\rm E} \lesssim 0.02$.

For either mass and accretion ratio scenario, the observed AGN UVOIR spectrum has a shape unlike that expected from a pure disc, but quite similar to that expected from reprocessing in the BLR (see e.g. D. Lawther et al. 2018). In particular it rises towards longer wavelengths and, although the spectral resolution is limited, it has bumps at 3000–4000 Å, and at ∼ 7000–8000 Å, where emission from the Balmer and Paschen continua, respectively, are expected. Given also the very high correlation between the X-ray and other wavebands, we conclude that the most likely source of the UVOIR variations is the BLR, which has a direct line of sight to the X-ray source.

5 PHYSICAL LAG MODELS

In this section we test whether the observed lag spectrum can be reproduced by theoretical reprocessing models. Using the SED and $\dot{m}_{\rm E}$ estimates from Section 4, we evaluate several geometries to determine which physical scenario best explains the wavelength-dependent delays. Although the evidence presented above indicates that the most likely source of the UVOIR radiation is the BLR, we also briefly consider here disc reprocessing (Section 5.1), which, until recently, was considered to be the 'gold standard' model. We also consider reprocessing from a 'bowl' geometry (Section 5.2), which attempts to fit simultaneously both the lag spectra and the SED before concluding with a short discussion of reprocessing from the BLR in the form of the RPC clouds model (Section 5.3).

5.1 KYNREVERB disc model

We first examine the standard thin-disc model as a baseline for pure disc reprocessing. The fully relativistic UV–optical disc thermal reverberation code package KYNREVERB has been used by E. S. Kammoun et al. (2021) to perform an in-depth exploration of AGN accretion disc lag spectra. To model the MCG +08–11–11 lag spectrum we set most of the parameters to the fiducial values given by E. S. Kammoun et al. (2021) so that the disc inner radius

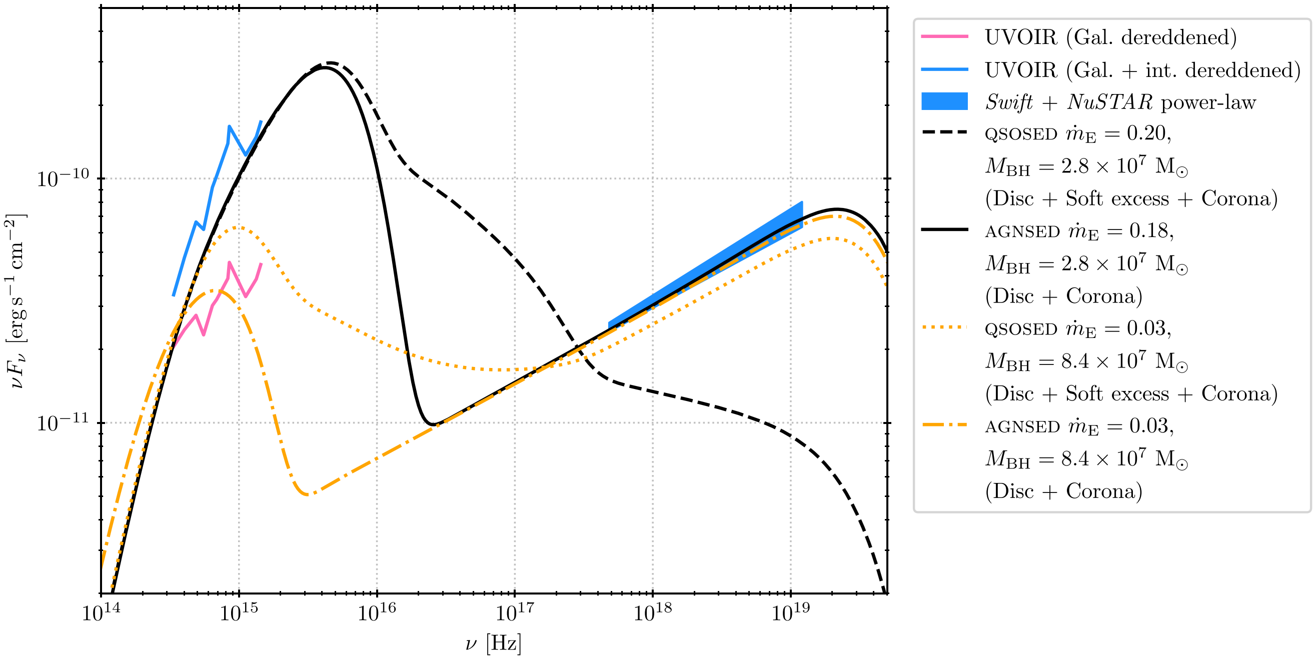

Figure 9. The broad-band SED of MCG +08–11–11. The black lines show model SEDs for a fixed black hole mass 2.82×10^7 M$_\odot$: the dashed black line shows the simple QSOSED SED for an accretion ratio $\dot{m}_\mathrm{E} = 0.20$; the solid black line shows the AGNSED SED for $\dot{m}_\mathrm{E} = 0.18$, fit to the X-ray spectrum and excluding a soft X-ray excess component (see Section 4.4 for details). The orange lines show model SEDs for a fixed black hole mass 8.4×10^7 M$_\odot$: the dotted orange line shows the QSOSED SED for $\dot{m}_\mathrm{E} = 0.03$; the dot–dashed orange line shows the AGNSED SED for $\dot{m}_\mathrm{E} = 0.03$. The pink curve shows the host–galaxy emission-subtracted UVOIR spectrum, corrected for Galactic dust reddening; the blue curve is additionally corrected for intrinsic reddening as described in Section 4.3. The blue quadrilateral marks the 3σ uncertainty region for a power-law fit to the 2–50 keV X-ray continuum, described in Section 4.1.

is determined by the innermost stable circular orbit, the corona height $h = 10$ R_g, and the system inclination is 40°. Following E. S. Kammoun et al. (2021), we set the disc colour temperature correction factor to $f_\mathrm{col} = 2.4$ across the whole disc. The colour temperature correction factor modifies both the shape and luminosity of the disc spectrum and was described in detail by C. Done et al. (2012).[8] In turn f_col modifies the lag spectrum: higher values of f_col give generally longer lags and greater curvature in the lag spectrum, with a much steeper UV–optical rise (see the discussion in section 4.2 of I. M. M$^\mathrm{c}$Hardy et al. 2023). In addition to fixing f_col to a specific value across the whole disc, it is also possible to implement a more physically motivated scheme in which f_col changes across the disc according to its temperature at each radius (following the prescription of C. Done et al. 2012). After some experimentation, we determine that a constant $f_\mathrm{col} = 2.4$ fits our observations best, since the additional curvature helps to match both the steep X-ray to UV lag and the flattening of the lag spectrum towards the infrared. Models without any such correction ($f_\mathrm{col} = 1$) or following the C. Done et al. 2012 prescription were unable to approximate the lags across the full observed wavelength range.

We run the models for both spin $a_\star = 0$ and 1 and in each case we simulate for a range of outer disc radii between 2000 and 10 000 R_g. The lags for our assumed mass and accretion ratio are shorter than the observed ones. The black hole mass is the parameter that has the greatest effect on the scale of the lags, and the estimated mass for MCG +08–11–11 is quite uncertain (a factor ≈ 3, M. M. Fausnaugh et al. 2017). Therefore, in addition to performing calculations for the fiducial mass 2.82×10^7 M$_\odot$, we additionally perform runs with the mass increased by a factor 2 and 3. The range of predicted lags for each mass and outer disc radius are shown in Fig. 10, for both spins $a_\star = 0, 1$. For $a_\star = 0$, a mass twice as large as the RM estimate and an outer disc radius $R_\mathrm{out} \approx 2500$ R_g (the orange dashed line in Fig. 10) we obtain a reasonable match to the scale and shape of the observed lag spectrum. Increasing the spin decreases the lag at each wavelength, so for $a_\star = 1$ an even higher mass can approximately match the observed lag spectrum with $R_\mathrm{out} \approx 2000$ R_g (the green dashed line in Fig. 10). The fact that higher masses produce lag spectra that are closer to the observations is consistent with the arguments earlier based on the overall SED, the X-ray spectrum, the accretion ratio, and the X-ray variability properties, which also argue in favour of a higher mass, from a different perspective.

In summary, the RM derived black hole mass appears too low to reproduce the observed lag spectrum using a GR thin disc lamp-post reprocessing geometry. Adopting a higher mass together with a large disc colour–temperature correction can yield lags of comparable overall scale, but the detailed wavelength dependence remains poorly matched. In the following subsection, we investigate an alternative disc geometry.

5.2 Bowl model

In the KYNREVERB model, the combination of a high black hole mass, large colour correction factor, and small disc outer radius were required to match the shape of the observed lag spectrum

---

[8] Although the form of f_col was derived in the context of stellar-mass black hole binary discs, its application was tested against full radiative transfer models for AGN discs and reasonably good agreement between the resultant disc spectra was found: see section 2 of C. Done et al. (2012).

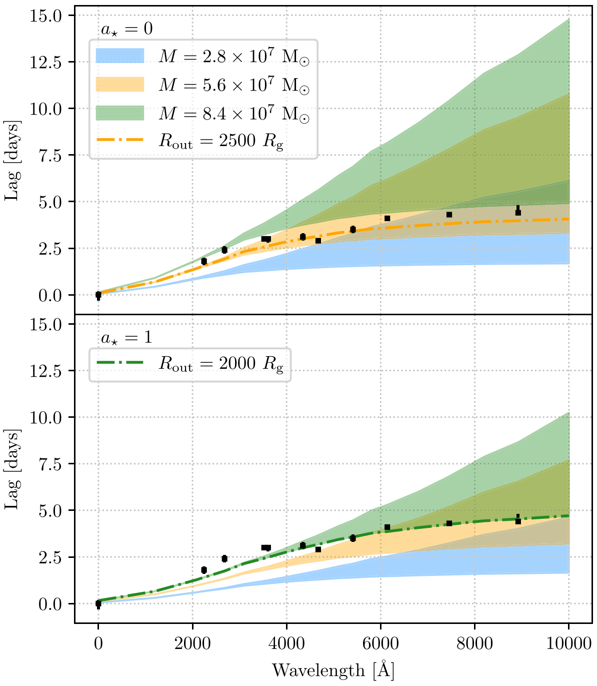

Figure 10. Lag spectra predicted by the model KYNREVERB (coloured regions) compared with the empirical lags determined by JAVELIN (black points). Lag spectra are calculated for the assumed black hole mass 2.82×10^7 M$_\odot$ (blue) as well as masses a factor of 2 and 3 greater (orange and green, respectively). The scale of the lags increases with mass. For each mass, lag spectra are generated for both zero spin (top panel) and maximum spin (bottom panel) and for a range of outer disc radii between 2000 and 10 000 $R_{\rm g}$. The dot–dashed orange line shows the predicted spectrum for a mass 5.6×10^7 M$_\odot$ and $R_{\rm out} = 2500\ R_{\rm g}$ in the zero spin case and dot–dashed orange line shows the predicted spectrum for a mass 8.4×10^7 M$_\odot$ and $R_{\rm out} = 2000\ R_{\rm g}$ in the maximum spin case.

(steep at short wavelengths, flattening at long). Another way to achieve this shape with a standard disc is with an alternative geometry, such as a ‘bowl-shaped’ accretion flow consisting of a flat disc that flares into a larger scale height wall beyond a certain radius (e.g. D. A. Starkey et al. 2023; R. Edelson et al. 2024). We assume the M. M. Fausnaugh et al. (2017) mass estimate (2.82×10^7 M$_\odot$) and run the model with the disc inner radius set to 6 $R_{\rm g}$, the corona height to 10 $R_{\rm g}$, and the system inclination to 45°. The disc rim height rises with radius as $H \propto R^{100}$. Fits to our ‘faint’ and ‘bright’ AGN SEDs [evaluated at X$_{\rm min}$ and X$_{\rm max}$ (Section 3.1) and dereddened as described in Section 4.3] are shown in Fig. 11. This model predicts a disc truncation radius of 5.90 ± 0.60 light days ($\approx 4000\ R_{\rm g}$) and a temperature there of ~ 2000 K, approximately the dust sublimation temperature (R. Barvainis 1987). The model fit to the faint SED gives an upper limit on the accretion rate $\dot{M} < 0.153$ M$_\odot$ yr^{-1} and $L/L_{\rm Edd} < 0.198$. The modelled lag spectrum is shown in the lower panel of Fig. 11. The model is able to reproduce the scale of the observed lags and the overall spectrum shape but still produces a smooth lag–wavelength relationship in contrast to the more complex pattern observed. A forthcoming version of this model includes an opacity-dependent rim height allowing the Bowl model to produce Balmer and Paschen edges in the lag spectrum (Sinha & Horne in preparation).

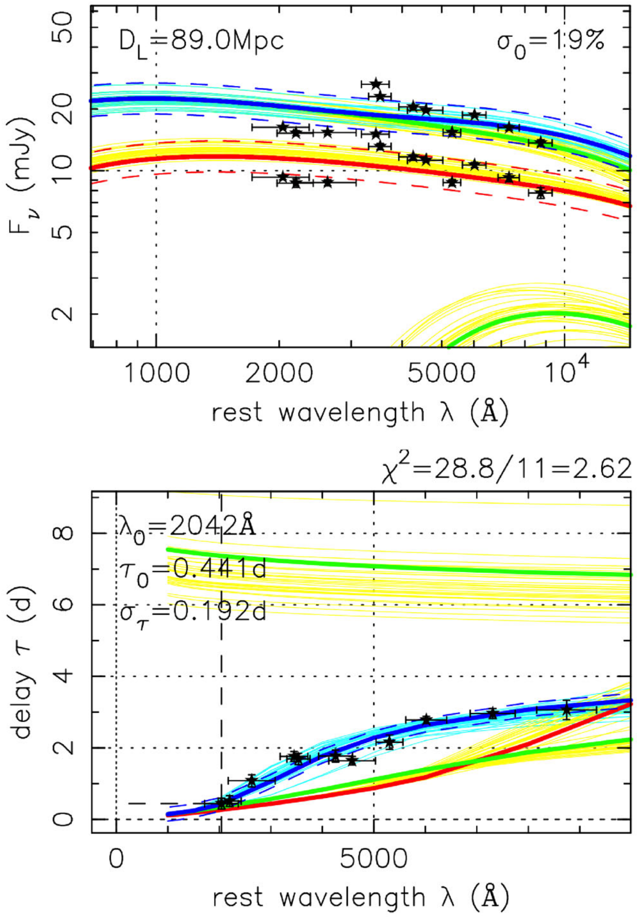

Figure 11. Bowl model analysis. The top panel shows the disc spectrum and the bottom panel shows the model lag spectrum (blue) compared with the measured one (black stars). The assumed black hole mass is 2.8×10^7 M$_\odot$ and the input faint and bright AGN SEDs have been dereddened for both Galactic and intrinsic reddening as described in Section 4.3. The red and blue curves give SED and lag predictions for the faint and bright states. The green curves give bright-state lags and SEDs separately for the flat disc and for the steep rim, inside and outside of the temperature minimum.

Since none of the disc models presented so far can account for the *u*- and *i*-band excess lags, we next test a model with an additional reprocessing component.

5.3 Radiation pressure confined clouds

In this subsection we test a model that also includes a reprocessing contribution from the BLR that can introduce additional structure into the lag spectrum. K. T. Korista & M. R. Goad (2001, 2019) have shown that incident high-energy emission, reprocessed in the BLR, can give rise not only to strong broad optical–IR recombination lines (the Balmer and Paschen series lines of hydrogen), but also a significant thermal diffuse continuum component (DC), which at UV–optical wavelengths is dominated by hydrogen free–bound recombination continuum (the Balmer and Paschen continuum), with a weaker contribution from free–free emission, and a strong Rayleigh scattering feature that dominates the diffuse continuum in the vicinity of Ly α. For example, in fig. 5 of K. T. Korista & M. R. Goad (2001), they show the lags that might

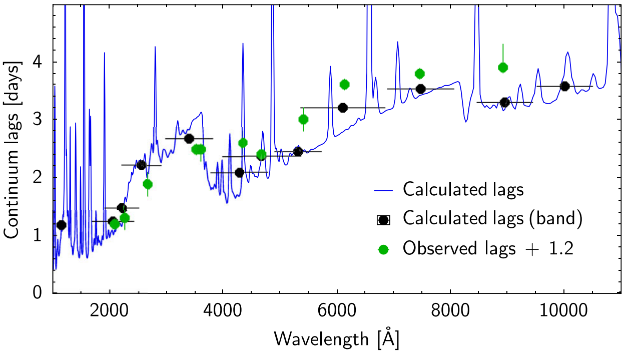

Figure 12. A fit to the lag observed spectrum (green points) with an RPC cloud model (similar to the models presented by H. Netzer et al. 2024 for Mrk 817). The full model lag spectrum (blue solid line) is dominated by the BLR. The black points show the mean model lags in several broad bands, for easier comparison with the observed ones.

be expected in the wavelength range 1000–7000 Å from NGC 5548 during two *HST* and *IUE* monitoring campaigns.

Recently H. Netzer (2020, 2022) has calculated similar lags under the assumption that the BLR is made up of RPC clouds. The clouds are irradiated by a combination of UV emission from the disc and X-ray emission from the central source. H. Netzer (2022) showed that, for a small sample of AGN, most of the observed lags could be reproduced by modelling the response of the BLR clouds, with only a minor contribution from the accretion disc (if any). A more detailed model of this type, applied to Mrk 817, is shown and discussed in H. Netzer et al. (2024). In Fig. 12 we show the full model prediction for MCG +08–11–11 over all wavelengths as a blue line. Our observed lags are shown as green circles. To allow easier comparison to our observations, the model lags averaged over the wavelength ranges of our observational bands are shown in black. In this RPC cloud model, the lags are calculated relative to the ionizing UV radiation and assuming an offset of 1 d relative to the 1100 Å continuum. In Fig. 12 the observed lags have been shifted by 1.2 d so that the shortest-wavelength lag (UVW2 2084 Å) approximately matches the relevant calculated lag in that band.

Over the UVOIR range covered by the modelling, and normalized to the UVW2 lags, the RPC cloud model and observed lags are in reasonable agreement. They agree particularly well in the regions of the Balmer and Paschen continua.

Taken together, the modelling in this section shows that a thin disc alone cannot reproduce the observed lag spectrum. The excess lags around *u* and *i* are highly suggestive of reprocessing by gas in the BLR. The flattening of the lag spectrum towards longer wavelengths may be due to a high colour temperature correction factor, or the onset of a large scale-height disc wind or flared disc. We discuss the implications our findings below in Section 6 and conclude in Section 7.

6 DISCUSSION

In this paper we have presented 12 very high-quality light curves of the bright Seyfert 1.5 AGN MCG +08–11–11 from X-ray to near-IR. Over a 3 month period we obtained on average more than two observations per day with *Swift* (X-ray and UV/optical) and better than daily cadence with ground-based observatories (optical and near-IR bands). From these data we have determined one of the best-defined AGN lag spectra yet produced. We measured lags relative to the *Swift* UVW2 band using two different methods (ICCF and JAVELIN) and obtained very consistent results. From flux–flux analysis of the light curves we have distinguished the separate SEDs of a constant galaxy component and a variable AGN component. We have analysed the combined *Swift*-XRT data from our observations with archival *NuSTAR* data to provide a 0.3–50 keV spectrum, which we have combined with the UVOIR AGN data to provide a multiband SED.

Many of the observational results are common to those from similar campaigns on other AGN. These include (i) UVOIR lags that increase with wavelength; (ii) a lag spectrum that is flatter than predicted by a simple disc reprocessing model; (iii) an X-ray/UV lag that is longer than one would expect from an extrapolation of the UVOIR lags (see Fig. 6); and (iv) ‘excess’ lags in bands covering the Balmer and Paschen jumps. However, in strong contrast to many previous studies, the X-ray and UVOIR light curves of MCG +08–11–11 are highly correlated. We find $r_{\max} = 0.85$ between the X-ray and UVW2 bands, which is, to the best of our knowledge, the strongest such correlation yet reported for an AGN. Additionally, while previous similar studies have found that the variable component has a shape consistent with a canonical, blue disc spectrum (e.g. E. M. Cackett et al. 2020; I. M. M$^{\mathrm{c}}$Hardy et al. 2023), here we find a much redder variable spectrum. If the variable spectrum relates to the AGN accretion disc, then this finding implies that either the disc is cool (likely requiring a high black hole mass), or that the emission is substantially reddened by dust within the host galaxy. Below, we briefly discuss the most important findings from this study.

6.1 The shape of the lag spectrum

In Section 3 we determined the lags between photometric bands using two methods: ICCF and JAVELIN. The lags produced by the two methods are almost identical. Particularly for our very well sampled data, we find no reason why the assumptions built into JAVELIN, such as interpolation assuming DRW variability, should produce incorrect lags. However, we discuss this matter in more detail in Appendix B.

We then modelled the lag spectrum with disc and bowl models. Both require an edge, e.g. produced by an obscuring gaseous or perhaps dusty disc wind, to flatten the lag spectrum at longer wavelengths. The disc model requires a high colour correction factor of 2.4 to introduce sufficient curvature in the lag spectrum so that it can fit both the rapid increase in lags at short wavelengths and the slower increase at long wavelengths. The effect of a disc edge and of the colour correction factor are discussed in detail following observations of NGC 4395 by I. M. M$^{\mathrm{c}}$Hardy et al. (2023). We also refer readers to E. S. Kammoun et al. (2021) where the effects on the lag spectrum of the variation of many parameters, including the outer disc radius, are discussed. We find that, to obtain a good fit to the lags with the disc model, a mass of two or three times greater than the optical RM mass of M. M. Fausnaugh et al. (2017) of $2.82 \times 10^7 \mathrm{M}_\odot$ is required (i.e. at the upper end of the RM mass uncertainty range).

Both disc and bowl geometries can provide a reasonable description of the overall scale and shape of the lag spectrum but they cannot explain the most prominent features, i.e. the excess lags in the *u* and $r - i$ bands. These excesses are, however, easily explained as the Balmer and Paschen continua, arising from reprocessing in the BLR gas (K. T. Korista & M. R. Goad 2001; D. Lawther et al. 2018; K. T. Korista & M. R. Goad 2019; H.

Netzer 2020, 2022). Here we obtain a good fit using the RPC cloud model of H. Netzer (2022). Reprocessing in the BLR, which is more distant than the disc regions associated with UVOIR reprocessing, has the advantage that the large lag between the X-ray variations and the UV variations, which is hard to explain in disc reprocessing without the maximum 2.4 colour correction factor, is automatically explained.

6.2 The shape of the broad-band SED

In Section 4.1 we modelled the time-averaged X-ray spectrum using data from our campaign, together with archival *NuSTAR* spectra observed at a similar time. We measured the X-ray spectral index up to 50 keV, finding a hard spectrum with $\Gamma = 1.697 \pm 0.008$ and determined the 2–10 keV X-ray luminosity. In Section 3.1 we used the flux–flux method to decompose the multiband photometry into constant and variable components, taken to represent the host galaxy and AGN emission, respectively. The lack of curvature in the flux–flux plots is most easily explained if the spectral shape of the variable component does not vary with luminosity. Similar linear flux–flux plots have been shown in many other studies (e.g. M. M. Fausnaugh et al. 2016; D. Starkey et al. 2017; I. M. M^{c}Hardy et al. 2018; J. V. Hernández Santisteban et al. 2020; F. M. Vincentelli et al. 2021; R. Prince et al. 2025). However, H. Netzer et al. (2024) showed that variations in *HST* STIS spectra in Mrk 817 were consistent with a bluer-when-brighter interpretation of the variable component, although E. M. Cackett et al. (2023) had previously found no curvature in the flux–flux plots derived from *Swift* light curves. In the case of MCG +08–11–11 there is no requirement for spectral variability in the variable component to explain our flux–flux plots. Therefore, as we do not have any spectra to allow for deeper investigation, we proceeded with the flux–flux decomposition as the best available bespoke determination of its AGN and host galaxy spectra.

In Section 4.3 we noted that the AGN UVOIR spectrum obtained from our flux–flux analysis was much fainter and redder than the canonical disc spectrum of a bright AGN of this RM mass. The soft X-ray spectrum of MCG +08–11–11 is known to be heavily absorbed beyond purely Galactic extinction and absorption features are seen in optical resonance lines, both indicating the presence of substantial gas within the host galaxy along our line of sight. Since dust may also be present along with this gas, we attempted to 'correct' the UVOIR spectrum for reddening due to dust inside MCG +08–11–11. After some experimentation, we found that extinction correction using a flat reddening curve with intrinsic $A_V = 1.05$ mag could correct the flux–flux UVOIR spectrum to a blue disc spectrum with $\dot{m}_{\rm E} \approx 0.2$. (We note that the determination of the intrinsic UVOIR SED is quite uncertain, since it incorporates both the limitations of the flux–flux analysis to produce the 'observed' spectrum, discussed above, and uncertainty in the dereddening procedure mentioned in Section 4.3.)

In Section 4.4 we combined the UVOIR and X-ray spectra to model the broad-band SED. We used the simple prescriptive QSOSED model to determine the expected SED for the RM mass and $\dot{m}_{\rm E} \approx 0.2$. By design this SED matches the Galactic + intrinsic dereddened UVOIR spectrum well, but it completely fails to match the X-ray data, predicting a much fainter and softer X-ray spectrum. It is possible to obtain a good fit to the broad-band data using the more flexible model AGNSED, in which the X-ray photon index is a free parameter. This model is shown by the solid black line in Fig. 9. This solution is energetically possible as the variable UVOIR power is less than the variable driving X-ray power, although the SED shape is unusual.

It has been established that the X-ray photon index is positively correlated with $\dot{m}_{\rm E}$ (e.g. G. Rizaliti, M. Young & M. Elvis 2009; A. Kubota & C. Done 2018)[9] and this relationship is hard-wired into the QSOSED model. The hard X-ray photon index we measure, $\Gamma = 1.697$, suggests a low accretion ratio of $\dot{m}_{\rm E} \approx 0.03$ (G. Risaliti et al. 2009), similar to the estimate of 0.05 from M. M. Fausnaugh et al. (2016) based on the 5100 Å luminosity. Given the inferred bolometric luminosity of MCG +08–11–11 (from hard X-rays and other indicators: see Appendix D), this much lower value of $\dot{m}_{\rm E}$ is only possible if the black hole mass is in fact a factor of a few greater than the RM estimate of M. M. Fausnaugh et al. (2017). A higher mass and low $\dot{m}_{\rm E}$ naturally explain the *observed* SED shape (without requiring substantial additional reddening) since the intrinsic UVOIR spectrum will be fainter and redder as the result of a dimmer and colder disc, and the expected X-ray spectrum will be much harder.

Given the factor ≈ 3 uncertainty in the RM black hole mass, we produce SED models for a mass at the upper end of this range, and $\dot{m}_{\rm E} \approx 0.03$. The QSOSED prediction (the dotted orange line in Fig. 9) does not quite match the data (the UVOIR spectrum corrected only for Galactic reddening, shown in pink), being too bright and blue in the UVOIR band and slightly underluminous in X-rays. With AGNSED we are able to increase the radius of the hot inner accretion flow to increase the X-ray luminosity at the expense of the UV, thereby achieving a better match to the data. This best overall fit, constrained mainly by the X-ray part of the SED, adopts a mass of $8.4 \times 10^7 {\rm M}_{\odot}$ a factor ≈ 3 greater than that of M. M. Fausnaugh et al. (2017), but consistent with some other indicators such as the X-ray variability properties (see Section 4.2). A. Kubota & C. Done (2018) find that an accretion ratio of $\dot{m}_{\rm E} \sim 0.02$, close to our current best estimate, is the approximate limit below which the soft excess and strong blue disc emission disappear, which may explain our observations[10] (e.g. G. Matt et al. 2006; A. R. Patrick et al. 2012). The lack of a strong disc component is perfectly consistent with the deduction, from the shapes of both the lag spectrum and the AGN SED as deduced by flux–flux analysis, that the large part of the variable UVOIR emission is reprocessed radiation from the BLR.

So, in summary, our analysis for Fig. 9 presents two possibilities:

(i) the RM mass is accurate, so the bolometric luminosity implies $\dot{m}_{\rm E} \approx 0.2$, for which the observed X-ray spectrum would be unusually hard and bright. Luminous UVOIR disc emission would be expected and so, to reduce that luminosity to the observed levels, substantial intrinsic reddening (above Galactic) would be required. Or,

(ii) the X-ray photon index is a reliable indication of a low accretion ratio ($\dot{m}_{\rm E} \approx 0.03$), which requires that the black hole mass is at the upper end of the uncertainty range on the RM estimate. The broad-band SED is closer to the expectations for an AGN of this (higher) mass and (lower) $\dot{m}_{\rm E}$. The expected UVOIR luminosity would be much lower, consistent with the observed values without any reddening above Galactic and consistent

---

[9] However, see S.-J. Chen et al. (2025) for a discussion of the significance of this correlation.

[10] In addition the high line-of-sight Galactic column density, $N_{\rm H} \approx 2 \times 10^{21}$ cm^{-2}, is a hindrance to the detection of the soft excess.

with a large fraction of the UVOIR luminosity arising from reprocessing of X-rays in the BLR.

6.3 Proposed geometry

We propose that MCG +08–11–11 is not, as was thought previously, a high accretion ratio AGN but is a low accretion ratio AGN ($\dot{m}_{\rm E} \approx 0.03$) with a relatively high mass, approaching 10^8 $M_{\odot}$. We found that the AGN UVOIR spectrum was faint and red, while the X-ray emission was relatively luminous. Without invoking reddening within MCG +08–11–11 to explain the faint, red UVOIR spectrum we can instead approximate the broad-band SED with a model in which the standard (geometrically thin, optically thick) disc does not extend all the way down to the innermost stable circular orbit. Instead, the inner flow is taken up by a relatively large hot X-ray-emitting region, meaning the standard disc is intrinsically UV-faint. The very high correlation between the X-rays and other wavebands shows that there is a direct line of sight to the reprocessor(s) and the shape of the lag spectrum and AGN SED show that the main reprocessor is the BLR. The hard X-ray spectrum is strongly absorbed below ≈ 2 keV. Additionally, brief sharp drops in X-ray flux are observed along with a hardening of the 0.3–10 keV spectrum (e.g. Fig. 5), likely as the result of increased obscuration by dense gas on small spatial scales. At least part of the absorption then probably occurs near the inner radius of the BLR where the gas density is high. The absorbing gas may be part of a failed radiatively accelerated dusty outflow (B. Czerny & K. Hryniewicz 2011): around the dust sublimation radius in the disc, a dusty wind is launched. The transition to dust-free clouds marks the onset of the inner BLR. Alternatively the wind could be a line-driven gaseous wind (D. Proga & T. R. Kallman 2004) as suggested for NGC 4395 (I. M. M$^{\rm c}$Hardy et al. 2023). The large scale height of the outflow/BLR presents a large solid angle to the primary continuum source, leading to a high luminosity in reprocessed radiation, and strong correlations between the driving and reprocessed continuum light curves.

This geometry is different to that suggested for NGC 5548 and NGC 4151 despite these two AGN having similar masses and accretion ratios to MCG +08–11–11 ($M_{\rm BH} \sim 4 \times 10^7$ $M_{\odot}$ and $\dot{m}_{\rm E} \sim 0.01$: R. Edelson et al. 2017, A. Kubota & C. Done 2018). Intensive *Swift* monitoring of other AGN, including these, has revealed that the delay of UV variations behind X-rays is often longer than predicted by a simple extrapolation of the UVOIR lag spectrum to the X-ray band (e.g. R. Edelson et al. 2017; I. M. M$^{\rm c}$Hardy et al. 2018; R. Edelson et al. 2019). For both NGC 5548 and NGC 4151 an inflated inner accretion disc has been invoked, which might scatter and delay the incident X-rays, reprocessing them into far-UV, which then illuminates the outer 'standard' disc (R. Edelson et al. 2017; E. Gardner & C. Done 2017). Similarly, in MCG +08–11–11 we see an X-ray/UV lag (≈ 2 d) that is too long to be plausibly interpreted as simply the light travel time between the corona and inner accretion disc. However, an intermediate reprocessor results in weak-to-modest X-ray/UV correlations that *are* seen in NGC 5548 and NGC 4151 ($r_{\rm max} \approx 0.4$–0.7) but *not* in MCG +08–11–11 in which the X-ray/UV correlation is very strong ($r_{\rm max} \approx 0.85$), requiring direct illumination of the reprocessor (BLR) by the X-rays.

We find evidence for multiple reprocessing components in MCG +08–11–11, with different components dominating at different times, possibly linked to changes in luminosity. C. Fian et al. (2023) monitored MCG +08–11–11 for 6 months. Their 2019–20 light curves show large-amplitude long-time-scale variations (Fig. 5), unlike ours (Fig. 1). C. Fian et al. also reported longer optical lags than those we measured and a luminosity four times higher. Detrending light curves can remove biases in the measured lags (W. F. Welsh 1999) and reveal short-term lags that would otherwise be obscured (e.g. I. M. M$^{\rm c}$Hardy et al. 2014, 2018; M. Pahari et al. 2020; F. M. Vincentelli et al. 2021; C. Lewin et al. 2023; R. Edelson et al. 2024). Detrending the light curves of C. Fian et al. (2023) did indeed reveal shorter lags that are consistent with ours. Detrending was unnecessary for our light curves, as they showed no significant long-term trends. This analysis shows that both short and long lags were present *concurrently* during the 2019–20 campaign although with the longer lags dominating during that brighter phase. However, the shorter lags dominated during our fainter 2021 observations. A fourfold increase in luminosity could double the inner radius of the BLR (e.g. M. C. Bentz et al. 2013), leading to longer lags and smoother light-curve variations and, if due to an increase in accretion rate, the inner disc radius might also reduce, allowing for shorter disc lags. Similar luminosity-dependent lag behaviour has been observed in other AGN, such as in Mrk 110 (F. M. Vincentelli et al. 2021, 2022), where two variable components (attributed to the disc and BLR) showed increasing lags with higher ionizing luminosity, consistent with an expanding BLR.

7 CONCLUSIONS

We monitored the AGN MCG +08–11–11 intensively for a period of 3 months with *Swift* (in X-rays and UV/optical bands) and ground-based observatories (in optical and infrared bands). The correlations between all observed wavelengths were strong and in particular the X-ray/UV correlation ($r_{\rm max} = 0.85$) is, as far as we are aware, the strongest yet reported for an AGN. This implies an unimpeded line of sight between the X-ray corona and the UVOIR reprocessor(s).

Throughout our monitoring period the target was relatively faint and the UVOIR lags we measured were shorter than those measured in a recent optical campaign during which the source was approximately four times brighter (C. Fian et al. 2023). We found that short lags (consistent with those we measured) were also present in those earlier data, after filtering out the longer term trends. These observations demonstrate that more than one source of UV/optical variability is present within MCG +08–11–11: at least one of these sources must be associated with reprocessing in the BLR, giving rise to the structure seen on short time-scales in both the lag spectrum and the rms flux spectrum. The origin of the longer term variations is unknown but may be associated with the temperature fluctuations observed in AGN accretion discs by J. M. M. Neustadt & C. S. Kochanek (2022).

We found that pure disc reprocessing models could not reproduce the complex shape of the lag spectrum, whereas an RPC cloud model (approximating the reprocessed emission from the BLR) broadly matched the observations. If indeed emission from the BLR dominates the lags, the long (≈ 2 d) lag between X-ray and UV light curves is more easily explained than in the disc reprocessing scenario, which would require either an extreme corona height or an intermediate reprocessor, which is inconsistent with the very strong X-ray/UV correlation.

If the optical RM black hole mass estimate of MCG +08–11–11 ($M_{\rm BH} = 2.82 \times 10^7$ $M_{\odot}$) is accurate, then its bolometric luminosity implies an Eddington accretion ratio $\dot{m}_{\rm E} \approx 0.2$, which should produce a high UV disc luminosity that is not seen. In this case, much of the UV disc emission must be 'hidden' by substantial reddening within MCG +08–11–11. The X-ray spectrum should also be much softer and less luminous than is observed (A. Kubota & C. Done 2018). Alternatively, if the hard X-ray spectrum is a reliable indicator of the accretion ratio, it suggests a much lower $\dot{m}_{\mathrm{E}} \approx 0.03$ in which case the black hole mass must be at the upper end of the RM mass uncertainty range (i.e. $M_{\mathrm{BH}} \gtrsim 8 \times 10^7$ $\mathrm{M}_{\odot}$). This low accretion ratio is consistent with the value ($\dot{m}_{\mathrm{E}} \sim 0.02$) below which A. Kubota & C. Done (2018) predict that the inner optically thick part of the disc disappears, drastically reducing the UVOIR contribution from any remaining parts of the disc. This prediction is in good agreement with our conclusion that the large majority of the shorter time-scale UVOIR variability comes from reprocessing in the BLR.

ACKNOWLEDGEMENTS

Thanks go to Carina Fian for providing the 2019–20 Wise optical light curves. DK and IM^cH acknowledge support from the UK Science and Technology Facilities Council (STFC) from grant ST/V001000/1. EMC and JAM gratefully acknowledge for analysis of the Zowada Observatory data from the NSF through grant AST-1909199. FMV ackowledges finiancial support from the European Union's Horizon Europe research and innovation programme through the Marie Skłodowska-Curie grant agreement No. 101149685. This work made use of data supplied by the UK Swift Science Data Centre at the University of Leicester. This work makes use of observations from the Las Cumbres Observatory global telescope network.

DATA AVAILABILITY

Data on which this work is based are available from the *Swift* archive[11] and the LCO archive.[12]

REFERENCES

Arévalo P., Uttley P., Kaspi S., Breedt E., Lira P., M$^{\mathrm{c}}$Hardy I. M., 2008, MNRAS, 389, 1479
Bahcall J. N., Kozlovsky B.-Z., Salpeter E. E., 1972, ApJ, 171, 467
Barvainis R., 1987, ApJ, 320, 537
Beard M. W. J. et al., 2025, MNRAS, 537, 293
Bentz M. C. et al., 2013, ApJ, 767, 149
Bertin E., Arnouts S., 1996, A&AS, 117, 393
Bianchi S., de Angelis I., Matt G., La Parola V., de Rosa A., Grandi P., Jiménez Bailón E., Piconcelli E., 2010, A&A, 522, A64
Blandford R. D., McKee C. F., 1982, ApJ, 255, 419
Brown T. M. et al., 2013, PASP, 125, 1031
Buisson D. J. K., Lohfink A. M., Alston W. N., Fabian A. C., 2017, MNRAS, 464, 3194
Burrows D. N. et al., 2005, Space Sci. Rev., 120, 165
Cackett E. M., Horne K., Winkler H., 2007, MNRAS, 380, 669
Cackett E. M., Chiang C.-Y., M$^{\mathrm{c}}$Hardy I., Edelson R., Goad M. R., Horne K., Korista K. T., 2018, ApJ, 857, 53
Cackett E. M. et al., 2020, ApJ, 896, 1
Cackett E. M., Bentz M. C., Kara E., 2021, iScience, 24, 102557
Cackett E. M., Zoghbi A., Ulrich O., 2022, ApJ, 925, 29
Cackett E. M. et al., 2023, ApJ, 958, 195
Cardelli J. A., Clayton G. C., Mathis J. S., 1989, ApJ, 345, 245
Carr R., Cinabro D., Cackett E., Moutard D., Carroll R., 2022, PASP, 134, 045002
Chen S.-J., Wang J.-X., Kang J.-L., Kang W.-Y., Sou H., Liu T., Cai Z.-Y., Su Z.-B., 2025, ApJ, 995,197
Cohen R. D., 1983, ApJ, 273, 489
Cooke B. A. et al., 1978, MNRAS, 182, 489
Cutri R. M. et al., 2003, 2MASS All Sky Catalog of point sources, Centre de Donnees astronomique de Strasbourg (CDS)
Czerny B., Hryniewicz K., 2011, A&A, 525, L8
de Vaucouleurs G., de Vaucouleurs A., Corwin H. G., Jr, Buta R. J., Paturel G., Fouque P., 1991, Third Reference Catalogue of Bright Galaxies, Springer New York
Done C., Davis S. W., Jin C., Blaes O., Ward M., 2012, MNRAS, 420, 1848
Duras F. et al., 2020, A&A, 636, A73
Edelson R. et al., 2015, ApJ, 806, 129
Edelson R. et al., 2017, ApJ, 840, 41
Edelson R. et al., 2019, ApJ, 870, 123
Edelson R., Peterson B. M., Gelbord J., Horne K., Goad M., M$^{\mathrm{c}}$Hardy I., Vaughan S., Vestergaard M., 2024, ApJ, 973, 152
Emmanoulopoulos D., Papadakis I. E., Dovčiak M., M$^{\mathrm{c}}$Hardy I. M., 2014, MNRAS, 439, 3931
Evans P. A. et al., 2009, MNRAS, 397, 1177
Event Horizon Telescope Collaboration, 2019, ApJ, 875, L1
Event Horizon Telescope Collaboration, 2022, ApJ, 930, L12
Fausnaugh M. M. et al., 2016, ApJ, 821, 56
Fausnaugh M. M. et al., 2017, ApJ, 840, 97
Fausnaugh M. M. et al., 2018, ApJ, 854, 107
Fian C., Chelouche D., Kaspi S., Sobrino Figaredo C., Lewis T., Catalan S., 2023, A&A, 672, A132
Flewelling H. A. et al., 2020, ApJS, 251, 7
Fukugita M., Ichikawa T., Gunn J. E., Doi M., Shimasaku K., Schneider D. P., 1996, AJ, 111, 1748
Gardner E., Done C., 2017, MNRAS, 470, 3591
Gaskell C. M., Goosmann R. W., Antonucci R. R. J., Whysong D. H., 2004, ApJ, 616, 147
Gordon K. D., Clayton G. C., Misselt K. A., Landolt A. U., Wolff M. J., 2003, ApJ, 594, 279
Guo H., Wang J., Cai Z., Sun M., 2017, ApJ, 847, 132
HEASARC, 2014, Astrophysics Source Code Library, record ascl:1408.004
Hagen S. et al., 2024, MNRAS, 534, 2803
Harrison F. A. et al., 2013, ApJ, 770, 103
Henden A. A., Levine S., Terrell D., Welch D. L., Munari U., Kloppenborg B. K., 2018, in American Astronomical Society Meeting Abstracts #232. p. 223.06
Hernández Santisteban J. V. et al., 2020, MNRAS, 498, 5399
Jaffarian G. W., Gaskell C. M., 2020, MNRAS, 493, 930
Jansen F. et al., 2001, A&A, 365, L1
Kammoun E. S., Dovčiak M., Papadakis I. E., Caballero-García M. D., Karas V., 2021, ApJ, 907, 20
Kara E. et al., 2021, ApJ, 922, 151
Korista K. T., Goad M. R., 2001, ApJ, 553, 695
Korista K. T., Goad M. R., 2019, MNRAS, 489, 5284
Koss M. et al., 2017, ApJ, 850, 74
Kubota A., Done C., 2018, MNRAS, 480, 1247
Lamastra A., Bianchi S., Matt G., Perola G. C., Barcons X., Carrera F. J., 2009, A&A, 504, 73
Lawther D., Goad M. R., Korista K. T., Ulrich O., Vestergaard M., 2018, MNRAS, 481, 533
Lewin C., Kara E., Cackett E. M., Wilkins D., Panagiotou C., García J. A., Gelbord J., 2023, ApJ, 954, 33
Li I-Hsiu J. et al., 2019, ApJ, 884, 119
Lien A. Y. et al., 2025, ApJ, 989, 161
Ma Q., Wu X.-B., Gu H., Wen Y., Fu Y., 2023, ApJ, 949, 22
Matt G., Bianchi S., de Rosa A., Grandi P., Perola G. C., 2006, A&A, 445, 451
M$^{\mathrm{c}}$Hardy I., 1988, Mem. Soc. Astron. Italiana, 59, 239
M$^{\mathrm{c}}$Hardy I. M., 2013, MNRAS, 430, L49
M$^{\mathrm{c}}$Hardy I. M., Papadakis I. E., Uttley P., Page M. J., Mason K. O., 2004, MNRAS, 348, 783

---

[11] https://www.swift.ac.uk/swift_live/index.php
[12] https://lco.global/documentation/data/archive/

M^{c}Hardy I. M., Koerding E., Knigge C., Uttley P., Fender R. P., 2006, Nature, 444, 730
M^{c}Hardy I. M. et al., 2014, MNRAS, 444, 1469
M^{c}Hardy I. M. et al., 2018, MNRAS, 480, 2881
M^{c}Hardy I. M. et al., 2023, MNRAS, 519, 3366
Miller J. A. et al., 2023, ApJ, 953, 137
Miller J. A., Cackett E. M., Goad M., Korista K. T., 2025, ApJ, 985, 75
Murphy K. D., Nowak M. A., 2014, ApJ, 797, 12
Mushotzky R. F., Edelson R., Baumgartner W., Gandhi P., 2011, ApJ, 743, L12
Netzer H., 2019, MNRAS, 488, 5185
Netzer H., 2020, MNRAS, 494, 1611
Netzer H., 2022, MNRAS, 509, 2637
Netzer H. et al., 2024, ApJ, 976, 59
Neustadt J. M. M., Kochanek C. S., 2022, MNRAS, 513, 1046
Osterbrock D. E., Ferland G. J., 2006, Astrophysics of Gaseous Nebulae and Active Galactic Nuclei, University Science Books
Osterbrock D. E., Shuder J. M., 1982, ApJS, 49, 149
Pahari M., M^{c}Hardy I. M., Vincentelli F., Cackett E., Peterson B. M., Goad M., Gültekin K., Horne K., 2020, MNRAS, 494, 4057
Panagiotou C., Kara E., Dovčiak M., 2022, ApJ, 941, 57
Patrick A. R., Reeves J. N., Porquet D., Markowitz A. G., Braito V., Lobban A. P., 2012, MNRAS, 426, 2522
Peterson B. M., 1993, PASP, 105, 247
Peterson B. M., Wanders I., Horne K., Collier S., Alexander T., Kaspi S., Maoz D., 1998, PASP, 110, 660
Peterson B. M. et al., 2004, ApJ, 613, 682
Petrucci P. O. et al., 2023, A&A, 678, L4
Polletta M. et al., 2007, ApJ, 663, 81
Ponti G., Papadakis I., Bianchi S., Guainazzi M., Matt G., Uttley P., Bonilla N. F., 2012, A&A, 542, A83
Poole T. S. et al., 2008, MNRAS, 383, 627
Prince R. et al., 2025, MNRAS, 541, 642
Proga D., Kallman T. R., 2004, ApJ, 616, 688
Risaliti G., Young M., Elvis M., 2009, ApJ, 700, L6
Roming P. W. A. et al., 2005, Space Sci. Rev., 120, 95
Runnoe J. C., Brotherton M. S., Shang Z., 2012, MNRAS, 426, 2677
Schlafly E. F., Finkbeiner D. P., 2011, ApJ, 737, 103
Sergeev S. G., Doroshenko V. T., Golubinskiy Y. V., Merkulova N. I., Sergeeva E. A., 2005, ApJ, 622, 129
Shakura N. I., Sunyaev R. A., 1973, A&A, 24, 337
Shappee B. J. et al., 2014, ApJ, 788, 48
Skrutskie M. F. et al., 2006, AJ, 131, 1163
Starkey D. et al., 2017, ApJ, 835, 65
Starkey D. A., Huang J., Horne K., Lin D. N. C., 2023, MNRAS, 519, 2754
Sun M., Grier C. J., Peterson B. M., 2018, Astrophysics Source Code Library, record ascl:1805.032
Tonry J. L. et al., 2012, ApJ, 750, 99
Tortosa A. et al., 2018, MNRAS, 473, 3104
Uttley P., M^{c}Hardy I. M., Papadakis I. E., 2002, MNRAS, 332, 231
Vaughan S., Edelson R., Warwick R. S., Uttley P., 2003, MNRAS, 345, 1271
Vincentelli F. M. et al., 2021, MNRAS, 504, 4337
Vincentelli F. M., M^{c}Hardy I., Hernández Santisteban J. V., Cackett E. M., Gelbord J., Horne K., Miller J. A., Lobban A., 2022, MNRAS, 512, L33
Ward J., Wilson A. S., Disney M. J., Elvis M., Maccacaro T., 1977, A&A, 59, L19
Welsh W. F., 1999, PASP, 111, 1347
Wright E. L. et al., 2010, AJ, 140, 1868
Yu Z., Kochanek C. S., Peterson B. M., Zu Y., Brandt W. N., Cackett E. M., Fausnaugh M. M., M^{c}Hardy I. M., 2020, MNRAS, 491, 6045
Zu Y., Kochanek C. S., Kozłowski S., Peterson B. M., 2016, ApJ, 819, 122

APPENDIX A: FLUX–FLUX ANALYSIS PROCEDURE

In Section 3.1 we separated the variable and constant spectral components by performing a flux–flux analysis. We initially calculate the mean spectrum $A_\nu(\lambda)$ and the rms spectrum $S_\nu(\lambda)$ from the data and its uncertainties $F_\nu(\lambda, t)$ and $\sigma(\lambda, t)$, respectively. We define

$$\mathrm{X}(\lambda, t) \equiv \frac{F_\nu(\lambda, t) - A_\nu(\lambda)}{S_\nu(\lambda)} \tag{A1}$$

and estimate the light-curve shape $\mathrm{X}(t)$ by taking a weighted average over all wavelengths:

$$\mathrm{X}(t) = \sum \mathrm{X}(\lambda, t) W(\lambda, t) / \sum W(\lambda, t), \tag{A2}$$

where the inverse-variance weights $W(\lambda, t) = (S_\nu[\lambda]/\sigma[\lambda, t])^2$. $\mathrm{X}(t)$ is then scaled such that $\langle \mathrm{X} \rangle = 0$ and $\langle \mathrm{X}^2 \rangle = 1$. Next, $\mathrm{X}(t)$ is fixed so $A_\nu(\lambda)$ and $S_\nu(\lambda)$ can be estimated by linear regression. The algorithm then iterates through calculating $\mathrm{X}(t)$ assuming $A_\nu(\lambda)$ and $S_\nu(\lambda)$ are known, then calculating $A_\nu(\lambda)$ and $S_\nu(\lambda)$ assuming $\mathrm{X}(t)$ is known, until convergence.

We can then extrapolate the flux–flux relations to a lower brightness level than sampled by the data. The vertical line $\mathrm{X}_{\rm gal}$ on Fig. 3 indicates the point at which the flux in the bluest band (UVW2) is just 1σ above zero. Reading off the other band fluxes

Table A1. Results from the flux–flux analysis in Section 3.1.

Filter (1)	$\lambda_{\rm eff}$ (2)	A_ν (3)	S_ν (4)	min. (5)	max. (6)	AGN (7)	Galaxy (8)	Dered$_{\rm Gal}$ (9)	Dered$_{\rm int}$ (10)
UVW2	2083.95	0.622 ± 0.002	0.088 ± 0.002	0.491	0.849	0.608 ± 0.012	< 0.012	5.083	3.833
UVM2	2245.03	0.685 ± 0.003	0.085 ± 0.003	0.559	0.904	0.586 ± 0.021	0.099 ± 0.021	4.952	3.822
UVW1	2681.67	1.483 ± 0.004	0.145 ± 0.004	1.269	1.855	0.994 ± 0.026	0.490 ± 0.026	2.958	3.798
U	3520.88	3.288 ± 0.005	0.334 ± 0.005	2.793	4.149	2.298 ± 0.037	0.990 ± 0.037	2.318	3.606
u	3608.04	2.902 ± 0.007	0.298 ± 0.008	2.461	3.667	2.045 ± 0.055	0.856 ± 0.055	2.294	3.569
B	4345.28	3.931 ± 0.006	0.331 ± 0.006	3.442	4.782	2.272 ± 0.043	1.659 ± 0.042	2.042	3.211
g	4671.78	5.129 ± 0.005	0.357 ± 0.005	4.601	6.047	2.452 ± 0.036	2.677 ± 0.036	1.920	3.047
V	5411.45	6.504 ± 0.009	0.350 ± 0.009	5.986	7.404	2.404 ± 0.066	4.101 ± 0.065	1.720	2.701
r	6141.12	11.483 ± 0.009	0.512 ± 0.011	10.724	12.801	3.521 ± 0.079	7.962 ± 0.079	1.602	2.410
i	7457.89	11.694 ± 0.016	0.605 ± 0.020	10.797	13.251	4.159 ± 0.137	7.535 ± 0.136	1.437	1.972
z	8922.78	14.230 ± 0.027	0.686 ± 0.031	13.215	15.994	4.711 ± 0.217	9.519 ± 0.215	1.297	1.627

Note. All wavelengths (in Å) and fluxes (in mJy) are given in the observed frame. Column (3) is A_ν, the mean spectrum; Column (4) is S_ν, the rms spectrum; Columns (5) and (6) are the minimum and maximum total fluxes; Column (7) is the AGN component and Column (8) is the constant host galaxy component. Column (9) gives the multiplicative factor to be applied to the observed fluxes to correct for Galactic reddening ($A_V^{\rm MW} = 0.568$ mag using the curve of J. A. Cardelli, G. C. Clayton & J. S. Mathis 1989). Column (10) gives the multiplicative factor to be applied to the observed fluxes to correct for intrinsic reddening in the host galaxy rest frame ($A_V^{\rm int} = 1.05$ mag using the curve of C. M. Gaskell et al. 2004: see Section 4.3 for details).

at X_{gal}, we are able to obtain an estimate of the host galaxy SED (shown in dark red in the right-hand panel of Fig. 3). The average AGN SED is then the average component minus the host galaxy SED (this is shown in pink in the right-hand panel of Fig. 3). The resulting SEDs for MCG +08–11–11 are given in Table A1.

APPENDIX B: ICCF AND javelin

In Section 3 we determined the lags between photometric bands using two methods: ICCF and JAVELIN. Here we briefly comment on the comparison between those methods.

To interpolate between gaps in the observations, JAVELIN assumes that the variations in the light curves can be described by a Damped Random Walk (DRW) model. The PSD of a variability process that is described by a DRW is flat at low frequencies, bending to a power law slope of index −2 at high frequencies. The DRW high-frequency slope is consistent with AGN observations in both the X-ray (e.g. I. M. M$^{\mathrm{c}}$Hardy et al. 2004, 2006) and Section 4.2 here, and optical R. F. Mushotzky et al. 2011; H. Guo et al. 2017) bands. However, AGN X-ray PSDs have power law slopes of about −1 at low frequencies (I. M. M$^{\mathrm{c}}$Hardy et al. 2004, 2006) and we are starting to see the same low frequency slopes in optical PSDs (M. W. J. Beard et al. 2025). However, our present data are very well sampled and any interpolation occurs within the high-frequency slope range of the PSDs so the use of a DRW should introduce no errors.

JAVELIN also assumes that the delayed light curves are smoothed (by a top-hat function), linearly scaled and shifted versions of the driving light curve. The top-hat function would be the correct function if the X-ray source were surrounded by a spherical reprocessor. While that will not be the case for a pure disc reprocessor, the BLR as a reprocessor would be close to that geometry. Therefore, in the present case, any uncertainty introduced by uncertainty in the reprocessing function is likely to be small. As noted above, the ICCF, which merely maximizes the correlation between two light curves and makes no assumptions about the form of the variability, gives results that are completely consistent with those of JAVELIN (see Fig. 6). We therefore assume that the assumptions that are built into JAVELIN do not substantially affect our estimated time lags.

APPENDIX C: DETRENDING OF THE 2019-20 WISE OBSERVATORY LIGHT CURVES

In Section 3.4 we reanalysed the 2019–20 Wise Observatory light curves, taken a year prior to our *Swift* campaign. To investigate whether the longer lags seen in the un-detrended Wise data are due to an additional longer time-scale Fourier component of the lag or whether they are due to an independent cause, we have measured how the lags change depending on the time-scale used in the detrending. For this investigation we used simple moving-average detrending. We first smoothed the input light curves with a simple boxcar and then subtracted the smoothed light curve from the original. We performed this investigation between the 4250 and 7320 Å light curves. We chose the 7320 Å rather than 8025 Å light curve as it is of higher S/N.

In Fig. C1 we show, as filled black circles, the lags from the detrended light curves as a function of the full-width of the boxcar. We have also measured the lags between the smoothed light curves, shown as open red squares. We do not include lags from light curves smoothed with boxcars larger than 40 d as there would be fewer than five independent data points in the light curves. We can, however, use the subtracted light curves resulting from longer time-scale moving average subtraction as the number of independent data points does not change. We also indicate, as a dashed green line, the lag measured from the original un-detrended light curves. The uncertainty on that lag is shown by the errorbar on a single green star. The abscissa value of that star has no meaning. We note that, for boxcars up to 80 d, the subtracted lags remain at about 1.5 d, exactly the same value as we obtained from the LOWESS filtering with 45 d filtering time. At the longest, 120 d, boxcar, the lag rises as the effect of the boxcar becomes minimal. Meanwhile, the lag from the smoothed light curves are all longer, around 4.8 d, just below the lag measured from unfiltered light curves.

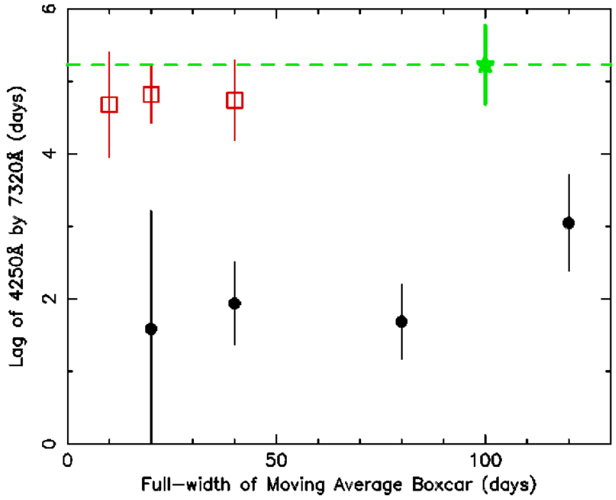

Figure C1. Lags resulting from detrending the 4250 and 7320 Å Wise light curves with a moving-average boxcar. The filled black circles are the lags from the detrended light curves and the open red squares are the lags from the smoothed light curves. The dashed green line is the lag measured from the original un-detrended light curves with the uncertainty shown by the single green errorbar, whose position on the x-axis has no relevance.

If we can assume that the short lags (1.5 d) measured in the detrended light curves are due to reprocessing, then the fact that these lags do not change even when time-scales as long as 80 d remain in the detrended light curves indicates that the short lags are not the result of removing longer time-scale Fourier components from the lag reprocessing function. The longer lags, which we see in the un-detrended light curves and in the smoothed light curves, are therefore probably the result of an independent process. We do not know what that process might be but J. M. M. Neustadt & C. S. Kochanek (2022) show that temperature fluctuations can move both inwards and outwards across the accretion disc producing both positive and negative lags on longer time-scales than reprocessing lags (~ 100 d, similar to those observed for MCG +08–11–11: C. Fian et al. 2023; Fig. 5). Moreover, the resultant slow flux variations dominate in amplitude over reprocessing variations. This may be the situation that we observe here.

APPENDIX D: DETERMINATION OF THE EDDINGTON RATIO

The flat X-ray spectrum of MCG +08–11–11 ($\Gamma \approx 1.7$ – see Section 4.1) suggests a lower Eddington accretion ratio than previously reported for this AGN, $\dot{m}_{\mathrm{E}} \approx 0.03$. Here, we investigate the

Table D1. Archival IR photometry.

Filter	λ (μm)	Magnitude	λF_λ (10^{-11} erg s^{-1} cm^{-2})
2MASS J	1.24	12.33 ± 0.05	5.7 ± 0.3
2MASS H	1.66	11.29 ± 0.05	6.6 ± 0.3
2MASS K	2.16	10.24 ± 0.03	8.2 ± 0.2
WISE W1	3.36	8.36 ± 0.02	15.1 ± 0.2
WISE W2	4.60	7.34 ± 0.02	13.7 ± 0.2
WISE W3	11.6	4.39 ± 0.01	13.0 ± 0.2
WISE W4	22.1	1.76 ± 0.01	23.2 ± 0.8

multiwavelength indicators of $\dot{m}_{\rm E}$ available for MCG +08–11–11, assuming the RM mass 2.82×10^7 M$_\odot$, as detailed below. The results are summarized in Table D2.

D1 Emission line estimates of $L_{\rm bol}$

Narrow emission lines may be used to estimate the bolometric luminosities of AGN and the method has been applied to samples of type 2 AGN for which direct measurements of the accretion disc continuum cannot be made. Because the narrow emission lines emanate from a large gaseous region beyond the AGN's dust torus they are less susceptible to extinction by dust in and around the central engine. However, the large size of the emission region therefore means that the lines only give an indication of the Eddington ratio averaged over very long time frames. From a fit to the mean optical spectrum of MCG +08–11–11 presented by M. M. Fausnaugh et al. (2017) from the 2014 RM campaign, we determine $\log(L_{\rm [O\,III]}/{\rm erg\,s^{-1}}) = 42.054 \pm 0.002$ and $\log(L_{\rm H\beta_n}/{\rm erg\,s^{-1}}) = 41.20 \pm 0.02$. (The luminosities have been corrected for Galactic dust extinction with $E(B - V) = 0.18$: E. F. Schlafly & D. P. Finkbeiner 2011.) A. Lamastra et al. (2009) provide a bolometric correction factor based on [O III] λ5007 for $\log(L_{\rm [O\,III]}/{\rm erg\,s^{-1}})$ in the range 42–44. From this factor and our measured $L_{\rm [O\,III]}$, we derive an Eddington ratio of $\dot{m}_{\rm E} = 0.14$. (This is reduced to 5 per cent if using the lower correction factor for $\log L_{\rm [O\,III]}$ in the range 40–42.) Using the luminosity-dependent narrow H β bolometric correction factor of H. Netzer (2019) and assuming a dust-free NLR, we again determine $\dot{m}_{\rm E} = 0.15$.

We note, however, that both the A. Lamastra et al. (2009) and H. Netzer (2019) bolometric conversions relate to line luminosities corrected for dust extinction within the NLR. We estimate the NLR dust extinction for MCG +08–11–11 using the Balmer decrement. R. D. Cohen (1983) gives the narrow-line flux ratio of H α to H β in MCG +08–11–11 as 5.40. Assuming an intrinsic narrow-line Balmer decrement of 3.1 (D. E. Osterbrock & G. J. Ferland 2006), we estimate that $E(B - V) \approx 0.55$ mag is required to produce the observed ratio. For a Milky Way type reddening curve (e.g. J. A. Cardelli et al. 1989) the intrinsic line luminosities $L_{\rm [O\,III]}$ and $L_{\rm H\beta}$ are a factor 5.8 and 6.2 higher than the observed ones, respectively (i.e. $\log(L_{\rm [O\,III]}/{\rm erg\,s^{-1}}) = 42.817 \pm 0.002$ and $\log(L_{\rm H\beta_n}/{\rm erg\,s^{-1}}) = 41.99 \pm 0.02$). The estimated Eddington ratios are, of course, increased by the same factors.

D2 X-ray estimates of $L_{\rm bol}$

From our fit to the time-averaged *Swift* X-ray spectrum, combined with the 2021 *NuSTAR* spectra (Section 4.1), we determined the 2–10 keV X-ray continuum luminosity to be $\log(L_{\rm X}/{\rm erg\,s^{-1}}) = 43.68$. Applying the F. Duras et al. (2020) luminosity-dependent bolometric correction factor we determine $\dot{m}_{\rm E} = 0.23$.

The *Swift* BAT 157-month hard X-ray survey (A. Y. Lien et al. 2025) reports a luminosity $\log(L_{\rm X}/{\rm erg\,s^{-1}}) = 44.13$ in the 14–195 keV band. This value is derived from the time-averaged spectrum generated from first 13 yr of BAT observations (from 2004 December). The estimation has the advantage that hard X-rays are not susceptible to moderate levels of photoelectric absorption. M. Koss et al. (2017) provide a simple bolometric correction factor $\kappa_{\rm bol} = 8$ for BAT luminosities from which we determine $\dot{m}_{\rm E} = 0.31$ although we note that this is an approximate correction, independent of the source luminosity.

D3 Infrared continuum estimates of $L_{\rm bol}$

It is also possible to estimate the bolometric luminosity from infrared wavelengths which probe the large-scale dust torus surrounding the AGN central engine. The dust readily absorbs and re-emits X-ray, UV, and optical photons, which make up the vast majority of an AGN's radiative output. The dust emission is therefore an effective bolometer for the AGN central engine. Because the torus is a very large scale structure ($\gtrsim$ pc or $\gtrsim$ 3 light years), the derived bolometric luminosity is an average over a long time scale (up to ∼decades)

We queried the *Wide-field Infrared Survey Explorer* (*WISE*; E. L. Wright et al. 2010) source catalogue and the 2MASS All-sky Point Source Catalog (R. M. Cutri et al. 2003; M. F. Skrutskie et al. 2006), both hosted on the Infrared Science Archive,[13] to obtain IR magnitudes of MCG +08–11–11. The *WISE* photometry relates to observations taken during the main survey (2009 December–2010 August); the 2MASS survey was conducted between 1997 June and 2001 February. The IR photometric magnitudes are listed in Table D1.

We derive infrared luminosities from the *WISE* W3 (12 μm) and W4 (22 μm) magnitudes, and the K-band (2 μm) magnitude from 2MASS. We use the luminosity-dependent infrared bolometric corrections of J. C. Runnoe et al. (2012) (see Table D2) and determine Eddington ratios which decrease with wavelength from 0.96 to 0.21. It should be noted that the infrared magnitudes have not been corrected for any host galaxy contamination. Although it has been noted that for quasars the infrared emission from the host galaxy typically becomes dominant only at wavelengths longer than 24 μm (J. C. Runnoe et al. 2012 and references therein), the same may not be true for Seyferts such as MCG +08–11–11 which have much lower AGN luminosities. The apparent increase of the Eddington ratio with wavelength may then be attributed to increasing host galaxy contribution to the infrared flux. We may then consider the shorter-wavelength (K and J) IR estimates of $\dot{m}_{\rm E} \sim 0.20$ to be the more reliable.

---

[13] https://irsa.ipac.caltech.edu/

Table D2. Various estimates of the Eddington ratio $\dot{m}_{\mathrm{E}}$.

Estimator	Bolometric correction	κ_{bol}	$\log(L_{\mathrm{obs}})$	$\log(L_{\mathrm{bol}})$	$\dot{m}_{\mathrm{E}} = L_{\mathrm{bol}}/L_{\mathrm{Edd}}$
22.19 μm (W4)	J. C. Runnoe, M. S. Brotherton & Z. Shang (2012) eqn. 8	16	44.33	45.53	0.96
12.08 μm (W3)	J. C. Runnoe et al. (2012) eqn. 6	11	44.14	45.20	0.45
2.16 μm (K)	J. C. Runnoe et al. (2012) eqn. 3	10	43.85	44.86	0.21
1.24 μm (J)	J. C. Runnoe et al. (2012) eqn. 2	22	43.63	44.98	0.27
H $\beta_{\mathrm{n}}\lambda$4861	H. Netzer (2019) table 1	3288 (4561)	41.20 (41.99)	44.72 (45.64)	0.15 (1.23)
[O III] λ5007	A. Lamastra et al. (2009)	454	42.054 (42.817)	44.71 (45.47)	0.14 (0.83)
2–10 keV	F. Duras et al. (2020) table 1	17	43.68	44.91	0.23
14–195 keV	M. Koss et al. (2017)	8	44.13	45.03	0.31

Note. Luminosities are in units of erg s^{-1}. For an assumed mass of 2.82×10^{7}~$\mathrm{M}_{\odot}$ the Eddington luminosity is $\log(L_{\mathrm{Edd}}/\mathrm{erg\,s^{-1}}) = 45.55$. For H β_{n} and [O III] numbers in parentheses include a correction for dust extinction in the NLR, as described in Section D1.

This paper has been typeset from a TEX/LATEX file prepared by the author.